THE ASTROPHYSICAL JOURNAL, 406:528–547, 1993 April 1

DENSE CORES IN DARK CLOUDS. VIII. VELOCITY GRADIENTS

A. A. GOODMAN[1]
Astronomy Department, University of California, Berkeley, CA 94720
P. J. BENSON
Wellesley College, Department of Astronomy, Whitin Observatory, Wellesley, MA 02181
AND
G. A. FULLER AND P. C. MYERS
Harvard-Smithsonian Center for Astrophysics, 60 Garden Street, Cambridge, MA 02138
Received 1992 June 3; accepted 1992 September 28

ABSTRACT

We present an analysis of motions consistent with uniform rotation in dense cores (density $\gtrsim 10^4$ cm^{-3}; size ~ 0.1 pc). Twenty-nine of the 43 cores studied have a statistically significant gradient. The detected gradients range in magnitude from 0.3 to 4 km s^{-1} pc^{-1}, corresponding to $2 \times 10^{-3} < \beta < 1.4$, with typical values $\beta \sim 0.02$, where β is the ratio of rotational to gravitational energy.

Some gradients are spatially continuous and are consistent with uniform rotation, but other apparent gradients are caused by clump-clump motion, or sharp localized gradients, within a map. The motions in L1495, B217, L1251, L43, B361, and L1551 are discussed in detail. In L1551, the residuals of the fit to the NH_3 velocity field indicate an outflow from IRS 5 in the same direction as the CO outflow.

Gradient orientation appears to be preserved over a range of density, as evidenced by comparing results for NH_3 to fits of $C^{18}O$ and CS maps. There appears to be no correlation between the inferred rotation axis and the orientation of elongated cores, a result consistent with the relatively small energy of rotation in these regions. The magnitude of the velocity gradient in a core has no relation to the absence or presence of an associated young stellar object.

We find that the specific angular momentum, J/M, scales roughly as $R^{3/2}$, where R represents the diameter of the FWHM intensity contour in a map. This relationship between specific angular momentum and cloud size can be understood if (*a*) cores are in approximate virial equilibrium, (*b*) line width scales as cloud size roughly according to $\Delta v \propto R^{1/2}$, and (*c*) β is roughly constant (i.e., independent of R) over the range of scales studied.

Subject headings: ISM: clouds — ISM: kinematics and dynamics — ISM: molecules — stars: formation

1. INTRODUCTION

About 100 dense cores have been mapped in the $(J, K) = (1, 1)$ transition of NH_3, revealing condensations with typical density $\gtrsim 10^4$ cm^{-3}, temperature ~ 10 K, narrow line widths ($\Delta v_{\rm FWHM} \sim$ several tenths of km s^{-1}), and size ~ 0.1 pc. These cores are often associated with very young stars (e.g., Myers & Benson 1983; Beichman et al. 1986), although the details of the process by which a core forms a star (or stars) are not yet definitively known (see Shu, Adams, & Lizano 1987 for a review). One crucial aspect of the star formation process in cores is the initial angular momentum of the core. This parameter bears on the final angular momentum of a star-disk system which may form in the core, on the support of the core itself, and on its potential for fragmentation (cf. Field 1978; Stahler 1983a, b; Cassen, Shu, & Terebey 1985; Larson 1985; Nakano 1984; Terebey, Shu, & Cassen 1984; Adams & Shu 1986; Tomisaka, Ikeuchi, & Nakamura 1988a, b, 1989, 1990; Kiguchi et al. 1987; Boss 1987, 1988, 1989; Mouschovias 1991; Tomisaka 1991).

The extensive velocity information contained in spectral-line maps provides the opportunity to analyze motions in molecular clouds carefully, and thus to estimate accurately the magnitude of "solid-body" rotation (i.e., rotation with uniform angular velocity about a fixed axis). To date, the most systematic studies of rotation in molecular clouds have come primarily from analyses of ^{13}CO spectral-line maps of dark clouds (Arquilla 1984; Arquilla & Goldsmith 1985; Goldsmith & Arquilla 1985; Arquilla & Goldsmith 1986). These studies focus on the larger and less dense clouds surrounding cores, with sizes ~ 10 core diameters, and average densities $\sim 10^3$ cm^{-3}, about one-tenth that of cores. Also, many substantial (e.g., ~ 10 km s^{-1} pc^{-1}) velocity gradients have been detected in interferometric observations of dense cores more massive than those studied here (cf. Harris et al. 1983; Armstrong, Ho, & Barrett 1985; Wadiak et al. 1985; Zheng et al. 1985; Ho & Haschick 1986; Jackson, Ho, & Haschick 1988).

In most analyses of dense core gradients, the velocity gradient is determined by taking an "appropriate" cut through the data and measuring the slope of a graph of line-center velocity versus map position offset. In the analysis presented here, we use more of the data in a map at once, by least-squares fitting maps of line-center velocity for the true direction and magnitude of the best-fit velocity gradient. (Menten et al. 1984 and Menten & Walmsley 1985 also employ a similar procedure in their analyses of Barnard 335 and Lynds 1551). In this paper we apply our gradient fitting technique to more than 40 cores, many of which have only recently been mapped (e.g., Benson & Myers 1989, hereafter BM). With this large sample, we are able

[1] Present address: Department of Astronomy, Harvard University, 60 Garden Street, Cambridge, MA 02138.

to make statistically valid statements about the role of rotation in the support and dynamics of dense cores.

Section 2 describes the fitting procedure, and the data set used. Section 3 presents the results of the fits, with particular attention to understanding the different morphologies (e.g., a smooth gradient versus clump-clump motion) which can give rise to gradients. The individual cores B217, L1495, L1251, L43, and L1551 are also discussed in some detail in § 3. In § 4 we examine relations among gradient orientation and cloud orientation, cloud elongation, and the presence or absence of a young stellar object (YSO). Section 5 compares results with gradients found in maps made with tracers other than NH_3. The gradient directions found in CS and $C^{18}O$ maps (from Fuller 1989) are consistent with the NH_3 direction. Also in § 5, NH_3 results are compared with ^{13}CO results in the B361 cloud (from Arquilla & Goldsmith 1985, 1986). The energetic role of rotation in dense cores is discussed in § 6, where we calculate β, the ratio of rotational to gravitational energy, for all the cores studied. The value of β is typically ~ 0.1, and rotation does not dominate the support of cloud cores.

2. FITTING AND DATA

2.1. *Least-Squares Fitting of a Velocity Gradient in a Spectral-Line Map*

In the spectral-line observations of interstellar gas clouds discussed here, the velocity, v_{LSR}, at the peak of a symmetric emission profile is assumed to represent an intensity-weighted average velocity along the line of sight through the cloud. If the cloud producing the emission line rotates as a solid body, v_{LSR} will be independent of distance along the line of sight, and linearly dependent on the coordinates in the plane of the sky. Thus, a cloud undergoing solid-body rotation can be expected to exhibit a linear gradient, ∇v_{LSR}, across the face of a map, perpendicular to the rotation axis, $\hat{\omega}$ (see the Appendix).

By fitting the function

$$v_{LSR} = v_0 + a\Delta\alpha + b\Delta\delta \,, \tag{1}$$

which corresponds to a linear velocity gradient, we estimate the amount of solid-body rotation implied by the observed line of sight velocity field in a cloud. Here $\Delta\alpha$ and $\Delta\delta$ represent offsets in right ascension and declination, expressed in radians; a and b are the projections of the gradient per radian on the α and δ axes; and v_0 is the systemic velocity of the cloud, with respect to the local standard of rest. In the context of equation (1), the magnitude of the velocity gradient, in a cloud at distance D, is

$$\mathcal{G} \equiv |\nabla v_{LSR}| = (a^2 + b^2)^{1/2}/D \,, \tag{2a}$$

and its direction (the direction of increasing velocity, measured east of north) is given by

$$\theta_{\mathcal{G}} = \tan^{-1}\frac{a}{b} \,. \tag{2b}$$

We have created a program, VFIT, which performs a least-squares fit of equation (1) to the velocity field observed in a spectral-line map of a molecular cloud, and returns the magnitude of the gradient, its direction, and the errors in those quantities. The basic fitting routine can be found as "REGRES" in Bevington (1969). In VFIT, each observed value of v_{LSR} is weighted by $1/\sigma^2_{v_{LSR}}$, where $\sigma_{v_{LSR}}$ is the uncertainty in v_{LSR} determined by a Gaussian fit to the line profile. This uncertainty is based on the signal-to-noise ratio in the spectrum, the velocity resolution of the observation, and the FWHM line width, Δv, using a relation derived from the work of Landman, Roussel-Dupré, & Tanigawa (1982)

$$\sigma_{v_{LSR}} = 1.15\left(\frac{\sigma_T}{T}\right)(\delta_v \Delta v)^{1/2} \,, \tag{3}$$

where T is the peak of a Gaussian fit to the line profile, σ_T is the rms noise in the spectrum, and δ_v is the velocity resolution of the spectrum. [Note that in observations using an autocorrelator as a spectrometer, with unity weighting, $\delta_v = 1.21 \times$ (velocity per channel), as in BM.] In using this estimate of $\sigma_{v_{LSR}}$, we are assuming that the line profiles are well fitted by a Gaussian, as is almost always the case.

Several parameters are calculated in VFIT to estimate goodness of fit. These include an F-statistic; a multiple correlation coefficient, χ^2; the rms about the fit; and the formal errors in the gradient and its direction. In this paper we quote only the formal errors, $\sigma_{\mathcal{G}}$ and $\sigma_{\theta_{\mathcal{G}}}$, as we have established that the simple condition $\mathcal{G} \geq 3\,\sigma_{\mathcal{G}}$ ensures that a fit has sufficient significance. We tested this "3 σ" criterion by comparing several goodness-of-fit indicators. For example, we found that a correlation exists between the F-statistic and $\mathcal{G}/\sigma_{\mathcal{G}}$, with 3 σ corresponding to approximately the 95% confidence level in the F-test.

We also tested the 3 σ criterion by using VFIT to fit sets of random data which contained no gradient, to determine how often a 3 σ fit occurs. Using a simulated spectral-line map—where (1) the velocity field is represented by a Gaussian random variable with a dispersion of 0.1 km s^{-1} and a mean of 0 km s^{-1}, (2) the FWHM line width of each spectrum is 0.6 km s^{-1}, measured with 0.08 km s^{-1} resolution, (3) the temperature distribution is a two-dimensional Gaussian with FWHM size 5′ and a peak of 0.4 K, (4) the map size is 10′ × 10′, and (5) the rms noise level varies between 0.07 and 0.08 K—fewer than 1 in 10 trials produce a 3 σ fit. For maps where the map extent is smaller, in that it is closer to the FWHM cloud size, the likelihood of a chance 3 σ gradient increases above 10% but does not exceed 20%. The larger the map size compared with the cloud size, the smaller the likelihood of chance gradients.

As a result of these reliability tests, we find that "3 σ" does not imply its usual (>99%) confidence level, in that a fit with $\mathcal{G} = 3\,\sigma_{\mathcal{G}}$ has, in reality, about a 90% chance of being valid. Furthermore, simulations showed that maps with fewer than nine detections ($T \geq 3\,\sigma_T$) could not be fitted as reliably as larger maps, and we have not included results of any fits to fewer than nine points in this paper.

A least-squares fitting technique which uses all points in a map simultaneously, and essentially fits a plane (eq. [1]) to three-dimensional (α, δ, v_{LSR}) data, will often give far different results than the alternative technique where one makes a "cut" through the map on the plane of the sky, and fits a line to solve for the change in velocity along that direction. Section 3 contains velocity maps of several clouds, which clearly illustrate the potential for these two methods to produce very different results. In particular, in § 3.6, we discuss this problem in the case of the L43/RNO 90 cloud, whose rotation has been studied in detail by Mathieu et al. (1988) and Pastor et al. (1993).

2.2. *Data*

In this paper we present an analysis of velocity gradients in cores as observed in the (J, K) = (1, 1) rotation inversion transition of NH_3. Fuller, Goodman, & Myers (1993) will present

an analysis of rotation in several of the cores discussed here, based on CS and $C^{18}O$ mapping. Fuller et al. (1991) have already discussed the B5 core, and its velocity gradients, in detail.

Many of the spectral-line maps we fit in this paper are presented and discussed in BM. In that study, 149 dark cloud positions were surveyed for evidence of dense cores in the form of $(J, K) = (1, 1)$ NH_3 emission. Because of our restriction that any map to be fitted contain at least nine points, six of the 41 cores BM mapped are not included in this study. Since 1989, Ladd (1991) and Benson (1992) have extended some of the BM maps and mapped several new regions which are also included here.

Table 1 presents a list of the cores studied, the position of the peak of the NH_3 emission in the region, and information about core distance, velocity, line width, size, elongation, and orientation. [The (0, 0) positions for the maps shown in later figures are given in the figure captions.] The information in Table 1 is from BM, Benson (1992), and Ladd (1991).

3. RESULTS

3.1. *Gradients Fitted*

Table 2 presents the results of fitting equation (1) to the NH_3 spectral-line maps of the cores listed in Table 1. In about two-thirds of the cores, a velocity gradient is detected at or above the 3 σ level. Figure 1*a* shows the distribution of fit significance for 43 cores. Given the analysis presented in § 2.1 above, we expect that about three out of the 30 gradients which have $\mathcal{G}/\sigma_{\mathcal{G}} \geq 3$ occur by chance.

For those objects listed in Table 1 which show a better than 3 σ gradient, most of the fit results fall in the range 0.3 km s^{-1}

TABLE 1

NH_3 $(J, K) = (1, 1)$ MAPPING DATA

Cloudname	Ref.	N	Peak Position							v_{LSR}	Δv	Mass	Core Size, Orientation, Shape			
			D	R.A. (1950)			Dec. (1950)						Major FWHM	Minor FWHM	Major Axis	Axial Ratio
			[pc]	[h]	[m]	[s]	[°]	[']	["]	[km/s]	[km/s]	[$M_\odot$]	[pc]	[pc]	[°] E of N	
PER3	1	23	350	3	25	37.5	30	55	20	4.1	0.58	35	0.42	0.10	48	0.24
PER6	1	20	350	3	27	10.3	30	12	34	5.8	0.53	20	0.24	0.10	29	0.42
B5	2	35	350	3	44	28.7	32	44	30	10.2	0.55	140	0.72	0.29	8	0.39
L1489	2	21	140	4	1	45.0	26	11	33	6.6	0.49	2.1	0.09	0.06	-39	0.67
L1498	2	10	140	4	7	50.0	25	2	13	7.8	0.46	0.8	0.07	0.05	-46	0.72
L1495	2	59	140	4	11	2.7	28	1	58	6.4	0.47	.....	0.29	0.08	-50	0.29
L1495, NW	2	32	140	4	10	44.5	28	4	58	6.1	0.47	4.0	0.23	0.13	-50	0.55
L1495, SE	2	27	140	4	11	2.7	28	1	58	6.7	0.47	.....	0.10	0.08	-40	0.83
TAU11	3	15	140	4	14	33.9	27	56	0	6.7	.....	.....	0.13	0.09	32	0.67
TAU16	3	28	140	4	14	59.6	28	15	0	6.6	.....	.....	0.14	0.08	29	0.59
L1400G	2	24	170	4	21	12.1	54	52	20	3.4	0.51	6.4	0.16	0.08	-60	0.48
B217	2	33	140	4	24	42.5	26	11	13	6.9	0.61	2.6	0.09	0.05	46	0.52
L1524	2	19	140	4	26	26.0	24	29	26	6.5	0.60	1.2	0.10	0.07	17	0.71
L1400K	2	17	170	4	26	51.0	54	45	27	3.2	0.50	14	0.31	0.14	44	0.45
TMC-2A	2	15	140	4	28	54.0	24	26	27	5.9	0.52	4.1	0.09	0.07	-28	0.86
L1534 (TMC-1A)	2	20	140	4	36	31.2	25	35	56	6.3	0.50	13	0.18	0.11	-66	0.63
L1527	2	13	140	4	36	49.3	25	57	16	5.9	0.52	2.4	0.09	0.07	8	0.81
TMC-1C	2	37	140	4	38	34.5	25	55	0	5.2	0.45	20	0.25	0.09	-49	0.37
L1517B	2	12	140	4	52	7.2	30	33	18	5.7	0.49	0.7	0.07	0.05	52	0.81
L1582A	2	16	435	5	29	11.9	12	28	20	10.2	0.67	150	0.53	0.25	-17	0.48
B35A	2	22	435	5	41	45.3	9	7	40	11.8	0.98	48	0.75	0.29	21	0.39
L134A (Northern Clump Only)	2	17	100	15	50	58.1	-4	26	36	2.7	0.51	83	0.10	0.07	-11	0.71
L1696A	2	9	160	16	25	30.0	-24	12	32	3.3	0.57	6.1	0.17	0.04	25	0.22
L43/RNO90	2,3	62	160	16	31	46.3	-15	40	50	0.8	0.50	.....	0.19	0.10	73	0.51
L43	2	27	160	16	31	46.3	-15	40	50	0.7	0.50	53	0.19	0.10	-87	0.51
L260 (a.k.a. L255)	2	18	160	16	44	22.3	-9	30	2	3.5	0.44	21	0.11	0.05	63	0.48
L158	2	42	160	16	44	33.7	-13	54	3	3.9	0.53	33	0.38	0.18	-67	0.48
L234E	2	9	160	16	45	22.6	-10	51	43	3.0	0.60	0.6	0.09	0.07	-30	0.84
L234A	2	13	160	16	45	21.0	-10	46	33	2.9	0.48	4.8	0.13	0.10	-6	0.75
L63	2	22	160	16	47	21.0	-18	1	0	5.7	0.49	8.0	0.13	0.11	14	0.79
L483	3	17	200	18	14	50.5	-4	40	49	5.5	0.66	.....	0.17	0.16	89	0.97
L778	2	11	200	19	24	26.4	23	52	37	9.9	0.59	39	0.19	0.13	-67	0.69
L1152	2	12	440	20	35	24.0	67	43	53	2.4	0.57	12	0.36	0.20	39	0.57
L1082C	2	14	440	20	50	19.5	60	7	40	-2.6	0.53	24	0.29	0.22	7	0.74
L1082A	2	26	440	20	52	20.7	60	3	14	-2.2	0.57	160	0.90	0.38	47	0.43
L1082B	2	10	440	20	52	41.0	59	58	19	-2.3	0.49	19	0.29	0.24	48	0.83
L1174	2	10	440	20	59	46.3	68	1	4	2.8	0.85	170	0.35	0.20	71	0.59
L1172A	2	12	440	21	1	45.0	67	42	13	2.7	0.65	8.2	0.20	0.18	-7	0.88
B361	2	22	350	21	10	35.0	47	12	1	2.7	0.81	49	0.35	0.30	31	0.85
L1031B	2	21	900	21	45	32.0	47	18	13	3.9	1.05	760	1.05	0.73	-39	0.70
L1251A	2	32	200	22	29	34.1	74	58	51	-4.0	0.54	32	0.41	0.12	-81	0.28
L1251E	3	32	200	22	38	11.7	74	55	20	0.3	0.90	.....	0.36	0.18	-87	0.50
L1262A	2	13	200	23	23	32.2	74	1	45	3.9	0.56	3.3	0.15	0.08	-68	0.50

NOTE.—Line parameters, including v_{LSR}, are derived from 18 component fits to the NH_3 $(J, K) = (1, 1)$ spectra, as described in BM. The line widths in this table are not for an NH_3 molecule; they are for an "average" particle with mass $m_{av} = 2.33$ amu. Thus, correcting for the difference in the thermal line widths between NH_3 and the average particle (see Myers 1983),

$$\Delta v = \left(\Delta v_{NH_3}^2 - \frac{kT_K}{m_{NH_3}} + \frac{kT_K}{m_{av}} \right)^{1/2},$$

where m_{NH_3}, Δv_{NH_3}, and T_K represent NH_3 mass, FWHM line width, and kinetic temperature, respectively. Core mass, size, shape, and orientation are also defined as in BM. Missing entries are due only to lack of data.

REFERENCES.—(1) Ladd 1991; (2) BM; (3) Benson 1992.

TABLE 2

RESULTS OF GRADIENT FITTING

Cloudname	Gradient [km/s/pc]	Direction [deg E of N]	$\mathcal{G}/\sigma_{\mathcal{G}}$	$\mathcal{G} \times R$ [km/s]	β	J/M [km/s pc]
PER3	1.70 ± 0.09	80 ± 3	19	0.35	5.4E-02	2.88E-02
PER6	0.32 ± 0.07	32 ± 15	5	0.05	1.5E-03	3.13E-03
B5	0.50 ± 0.10	113 ± 8	5	0.23	1.3E-02	4.23E-02
L1489	0.61 ± 0.30	-111 ± 25	2	.....	.....	.....
L1498	0.52 ± 0.56	-34 ± 65	1	.....	.....	.....
L1495	2.89 ± 0.12	147 ± 2	24	0.44	.....	2.68E-02
L1495, NW	3.90 ± 0.20	-84 ± 3	20	0.66	1.4E+00	4.47E-02
L1495, SE	0.60 ± 0.30	12 ± 15	2	.....	.....	.....
TAU11	2.00 ± 0.53	138 ± 15	4	0.22	.....	9.68E-03
TAU16	2.01 ± 0.50	16 ± 15	4	0.21	.....	8.78E-03
L1400G	0.58 ± 0.20	76 ± 30	3	0.07	5.8E-03	3.38E-03
B217	1.05 ± 0.14	-63 ± 10	8	0.07	9.8E-03	1.87E-03
L1524	1.43 ± 0.41	57 ± 15	3	0.12	7.1E-02	4.03E-03
L1400K	0.88 ± 0.31	105 ± 19	3	0.18	3.6E-02	1.47E-02
TMC-2A	2.20 ± 0.60	-73 ± 14	4	0.17	4.4E-02	5.25E-03
L1534 (TMC-1A)	2.19 ± 0.38	27 ± 9	6	0.30	7.4E-02	1.64E-02
L1527	3.32 ± 0.62	-177 ± 13	5	0.26	1.6E-01	8.14E-03
TMC-1C	0.30 ± 0.07	129 ± 14	4	0.05	1.2E-03	3.33E-03
L1517B	1.52 ± 0.57	-62 ± 18	3	0.09	5.4E-02	2.13E-03
L1582A	0.51 ± 0.25	-116 ± 33	2	.....	.....	.....
B35A	1.06 ± 0.16	57 ± 7	7	0.49	1.8E-01	9.06E-02
L134A (Northern Clump Only)	2.00 ± 0.70	52 ± 18	3	0.17	2.3E-03	5.78E-03
L1696A	0.40 ± 0.70	165 ± 137	1	.....	.....	.....
L43/RNO90	1.31 ± 0.12	130 ± 6	11	0.18	.....	9.89E-03
L43	1.58 ± 0.16	88 ± 11	10	0.22	9.0E-03	1.23E-02
L260 (a.k.a. L255)	0.71 ± 0.38	-30 ± 30	2	.....	.....	.....
L158	0.12 ± 0.12	-66 ± 78	1	.....	.....	.....
L234E	1.70 ± 0.80	103 ± 31	2	.....	.....	.....
L234A	0.50 ± 0.40	87 ± 39	1	.....	.....	.....
L63	0.40 ± 0.10	3 ± 21	4	0.05	2.6E-03	2.50E-03
L483	1.90 ± 0.20	52 ± 6	10	0.31	.....	2.02E-02
L778	0.40 ± 0.50	-5 ± 44	1	.....	.....	.....
L1152	0.80 ± 0.20	163 ± 16	4	0.22	7.9E-02	2.42E-02
L1082C	0.27 ± 0.15	-29 ± 37	2	.....	.....	.....
L1082A	0.95 ± 0.09	85 ± 4	11	0.56	8.5E-02	1.32E-01
L1082B	0.66 ± 0.21	-150 ± 18	3	0.18	3.3E-02	1.96E-02
L1174	0.87 ± 0.32	-145 ± 19	3	0.23	6.3E-03	2.43E-02
L1172A	0.66 ± 0.18	-72 ± 14	4	0.13	2.8E-02	1.02E-02
B361	0.71 ± 0.18	-32 ± 14	4	0.23	2.5E-02	2.98E-02
L1031B	0.17 ± 0.09	5 ± 29	2	.....	.....	.....
L1251A	1.33 ± 0.07	-77 ± 8	19	0.29	4.4E-02	2.53E-02
L1251E	3.48 ± 0.11	-156 ± 2	32	0.89	.....	9.10E-02
L1262A	0.40 ± 0.30	58 ± 57	1	.....	.....	.....

$pc^{-1} \lesssim \mathcal{G} \lesssim 2.5$ km s^{-1} pc^{-1}. Figure 1*b* shows the distribution of the magnitudes of all of the significant ($\geq 3\ \sigma$) gradients fitted.

The distribution shown in Figure 1*b* is subject to several "selection effects." Very small gradients are difficult to detect in data sets with finite velocity resolution and a small number of points. Our sample of cores is drawn from a somewhat diverse population, with different line widths, map sizes, and signal-to-noise ratios, and we cannot estimate an exact analytical detection limit. The smallest gradient we *detect* is ~ 0.3 km s^{-1} pc^{-1} (in TMC-1C), and we expect that this value is representative of our "detection limit."

We have created histograms of gradient magnitude both including and excluding upper limits, and we find that the distributions are not significantly different. Since the upper limits ($=3\ \sigma_{\mathcal{G}}$) are often found in cores with relatively few data points, and are typically not smaller than the very small gradients we can fit (in cores with many data points), we exclude upper limits from this analysis.

Projection effects also influence the distribution shown in Figure 1*b*. If the angular velocity vector, $\boldsymbol{\omega}$, points in the direction given by $\hat{\boldsymbol{\omega}}$, then

$$\boldsymbol{\omega} = \frac{\mathcal{G}}{\sin i}\,\hat{\boldsymbol{\omega}}\,, \tag{4a}$$

where i is the inclination of $\boldsymbol{\omega}$ to the line of sight, and the position angle of $\hat{\boldsymbol{\omega}}$ is given by

$$\theta_{\hat{\boldsymbol{\omega}}} = \theta_{\mathcal{G}} + \frac{\pi}{2}\,. \tag{4b}$$

In any individual case there is no way of finding i from spectral-line mapping data. However, for a random distribution of orientations, $\langle \mathcal{G}/\sin i \rangle = (4/\pi)\langle \mathcal{G} \rangle$, where angle brackets denote an average value (Chandrasekhar & Münch 1950; Tassoul 1978). Thus, in a statistical sense, any "typical" values of ω ($=|\boldsymbol{\omega}|$) derived for the sample of clouds in this paper can be "corrected" for projection effects.

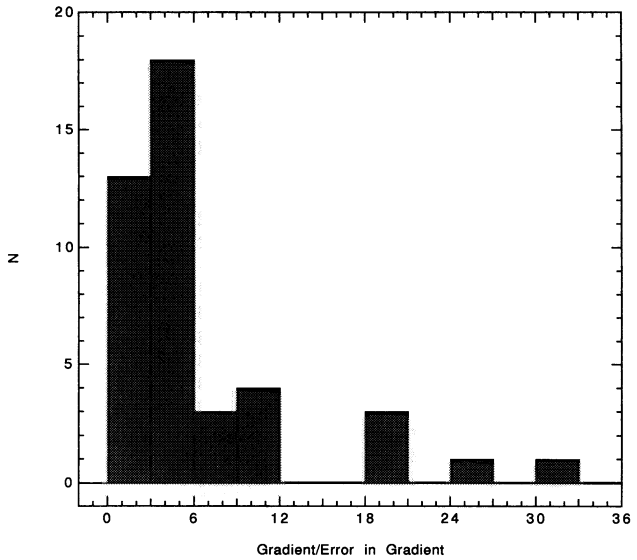

FIG. 1a

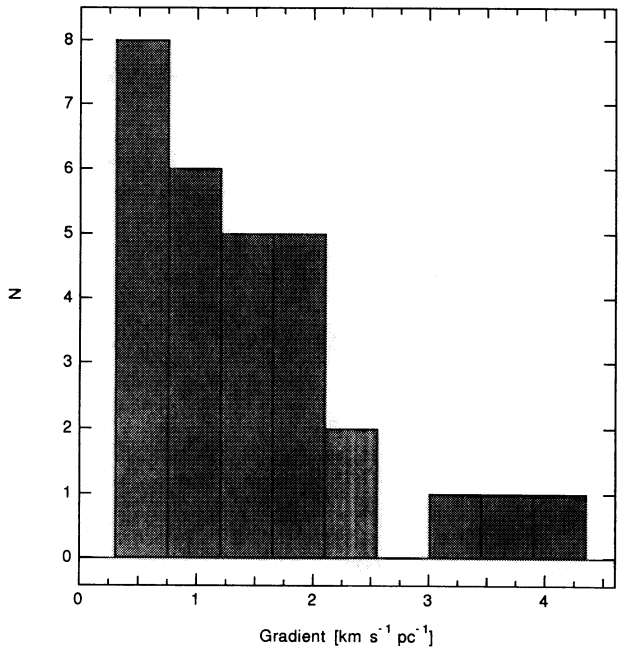

FIG. 1b

FIG. 1.—Distributions of (*a*) gradient significance and (*b*) magnitude ([*b*] and all figures to follow only include gradient with $\mathcal{G}/\sigma_{\mathcal{G}} \geq 3$).

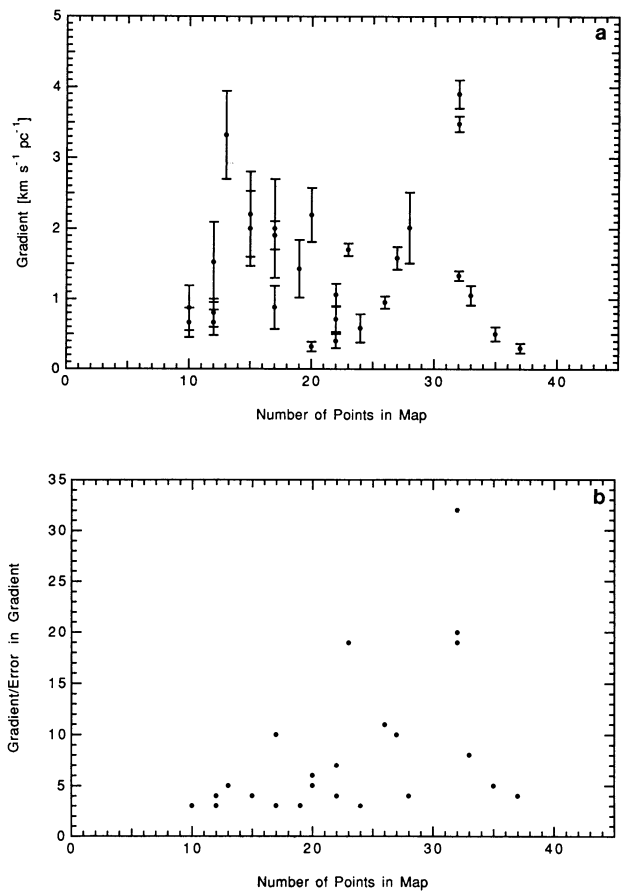

FIG. 2.—(*a*) Gradient magnitude and (*b*) significance, both as a function of the number of points in a map.

Figures 2*a* and 2*b* show the gradient, and the significance of the gradient, respectively, as a function of the number of points in the map. From Figure 2*b* it is clear that more highly significant gradients can be, *but are not necessarily*, fitted in maps with a large number of points. It is also evident that the absolute magnitude of the gradient and the number of points fitted are apparently uncorrelated (Fig. 2*a*). Therefore, we conclude that the distribution of gradients shown in Figure 1*b* is not significantly distorted by the number of points in each fit.

3.2. *Gradient Quality*

Figures 3*a* and 3*b* illustrate examples of what we call "good" gradients, where a smooth linear gradient exists over an entire map. In L1251A (Fig. 3*a*), a fit to 32 points produces a gradient whose magnitude is almost 20 times its error. Other clouds give even greater values of $\mathcal{G}/\sigma_{\mathcal{G}}$ (see Table 2), but clouds such as L1251A or B35A (shown in Fig. 3*b*) are special in that the gradient can be particularly easily identified (by eye) in a velocity map of $v_{\rm LSR}$.

Figure 3*c* (L158) illustrates an example of what we call a "bad" gradient, where the velocity map exhibits a seemingly random velocity field. In this case, VFIT returns $\mathcal{G} \approx \sigma_{\mathcal{G}}$, implying that no significant gradient can be found.

Velocity maps for the remainder of the cores listed in Table 1 illustrate the range between "good" and "bad."[2] In a typical case, many points will exhibit a pattern consistent with a gradient, but several other points will appear not to fit the pattern. The box-map presentation of the velocity field used in the figures can be deceptive because it does not take signal-to-noise ratio in the spectra into account. In the least-squares fitting, points which appear discrepant to our eye may be very heavily down-weighted, if they have a low signal-to-noise ratio (see § 2.1).

[2] Optical images and temperature contour maps of the majority of the cores in this paper can be found in BM.

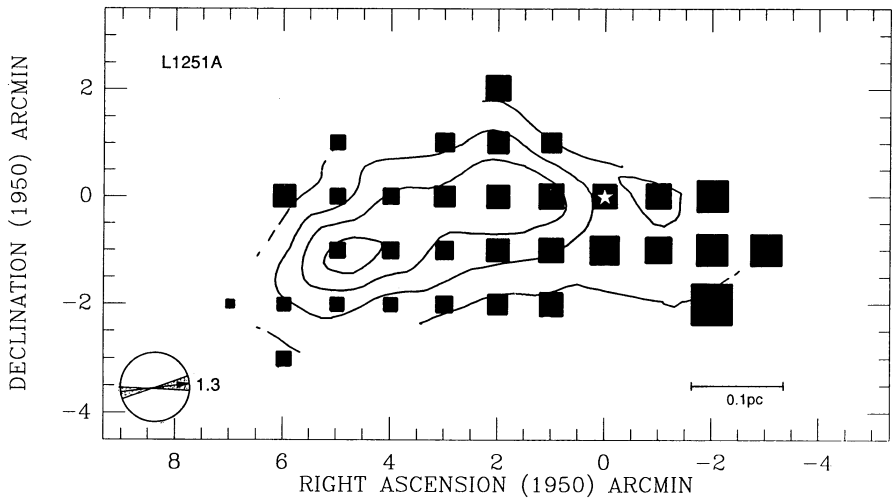

FIG. 3*a*

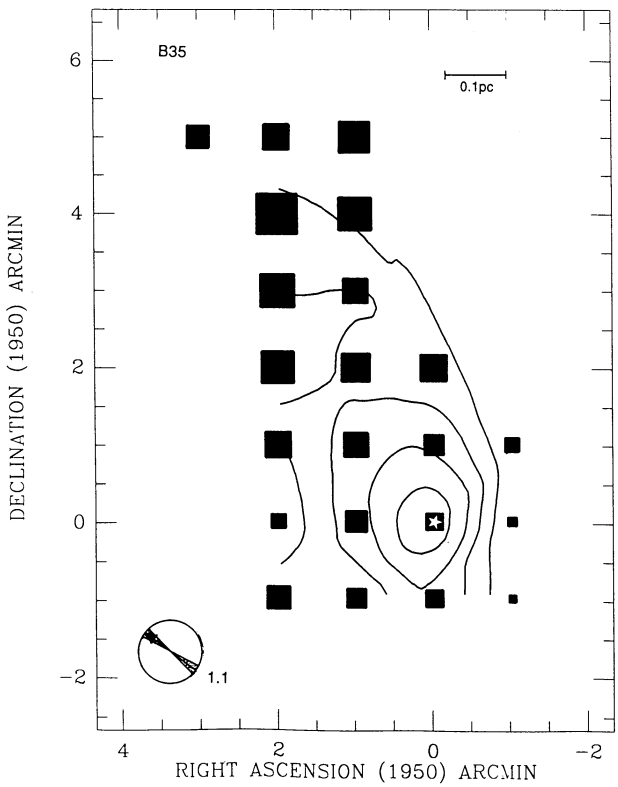

FIG. 3*b*

FIG. 3.—Filled squares of varying size represent the LSR velocity of the peak of the fitted NH_3 $(J, K) = (1, 1)$ line profile at each position, and contours map the peak antenna temperature. The linear size of a filled square is proportional to v_{LSR} at its position. The small circle with an arrow indicates the velocity gradient fitted to the NH_3 data (arrowhead points toward increasing v_{LSR}), and the shading around the arrow indicates the 1 σ error in the fit which determined the gradient. (A cross in the circle means that no significant gradient could be fitted.) Stars show the position of *IRAS* sources thought to be young stellar objects associated with these cores. The core names, (0, 0) map positions $(\alpha_{1950}, \delta_{1950})$, velocity ranges, and contour levels are as follows: (*a*) L1251A: ($22^h29^m03^s.2$, 74°58′51″), (−3.46, −4.65 km s^{-1}), (0.15, 0.35, 0.55, 0.75 K); (*b*) B35: ($05^h41^m45^s.3$, 09°07′40″), (11.28, 12.59 km s^{-1}), (0.15, 0.20, 0.25, 0.30 K); (*c*) L158: ($16^h44^m33^s.7$, −13°52′03″), (3.76, 4.16 km s^{-1}), (0.2, 0.3, 0.4, 0.5 K); (*d*) L1527: ($04^h36^m49^s.3$, 25°57′16″), (5.80, 6.39 km s^{-1}), (0.20, 0.35, 0.50 K).

3.3. *Gradients Caused by Local Effects within a Map*

The smaller maps are particularly susceptible to gradients caused by a few points near the edge of the mapped region. In L1527 (Fig. 3*d*), which contains only 13 data points, the velocity map suggests that the gradient fit would be reduced if the southernmost row of points were removed. In fact, if these three points are excluded, the formal gradient in L1527 goes from 3.3 ± 0.6 km s^{-1} (at −177° ± 13°) to 2.3 ± 0.9 km s^{-1} (at −152° ± 21°). The latter gradient does not pass our 3 σ test, but it is reassuring that its magnitude and direction are similar to those based on all the L1527 data.

The combination of our 3 σ and "≥9 points in a map" criteria should minimize, if not eliminate, the influence of these local effects.

3.4. *Motion of Clumps*

NH_3 mapping often reveals more than one clump within what may have previously been thought of as a single condensation. In Figures 4*a* and 4*b* we present maps of L1495 and B217, which clearly each contain two independent clumps, located so near to each other that mapping at lower resolution would not reveal them as separate. When considering velocity

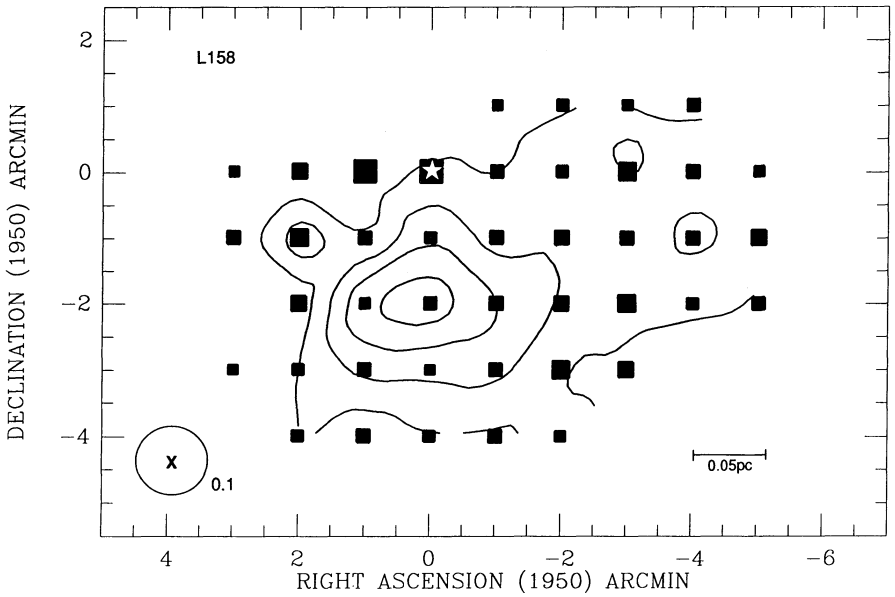

FIG. 3*c*

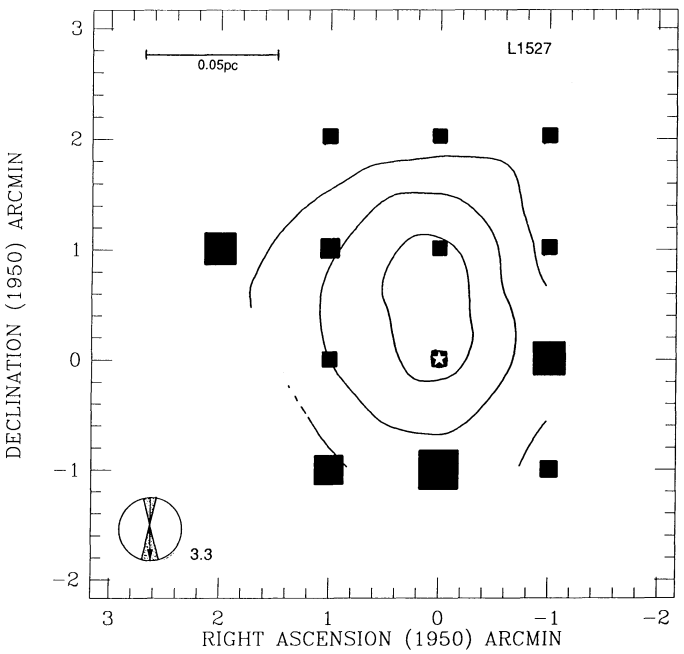

FIG. 3*d*

gradients in these clumpy clouds, we have the option to consider each clump as a separate entity or to fit the whole complex of clumps together.

Fitting each clump has advantages over fitting the entire complex if one wants to interpret gradients as rotation of an identifiable piece of a cloud. However, in comparing gradients measured in different tracers (e.g., NH_3 and CS), it is often useful to keep the size of the area sampled on the sky constant. In the case of L1495, for example, Fuller (1989) fits velocity gradients to CS and $C^{18}O$ maps, and his results clearly agree best with a fit to *all* of the NH_3 data contained within his map boundaries, rather than a single NH_3 clump. (Note that data for L1495 are presented in Tables 1 and 2 for the whole cloud together, and for each of the two clumps separately.)

Fitting a complex of clumps together often gives a very different result than fitting pieces individually. Figures 4*a* and 4*b* show that combinations of the gradients for the individual clumps labeled "L1495SE" and "L1495NW," or "B217NE" and "B217SW," clearly do not suggest the gradients fitted to all of L1495, or B217, respectively. Therefore, we are not just observing smaller pieces of a coherent larger scale linear gradient.

The mean LSR velocity of L1495SE differs from the mean in L1495NW by 0.6 km s^{-1}, more than twice a typical line width. The velocity map in Figure 4*a* makes it plain that these two clumps are kinematically distinct. Therefore, in fitting the NH_3 data for the "whole cloud," we are actually measuring the motion of one clump with respect to another, rather than a smooth gradient over the whole map. It is probable that maps of lower density tracers (such as $C^{18}O$), made over the same area, are actually sampling the bulk motion of the common "envelope" of the dense cores, each of which has a velocity gradient independent from that of the parent cloud.

In contrast, the mean velocities of the clumps in B217 differ by less than the typical (NH_3) line width (0.34 km s^{-1}), despite the fact that the LSR velocities of points near the center of the complex (shown as very dark in Fig. 4*b*) differ from the mean by more than 0.5 km s^{-1}. Rather than kinematically distinct blobs, as in L1495, the velocity profile in B217 shows a peak at the map center, giving rise to almost directly opposed gradient directions in the individual clumps.

In L1495 each subcondensation is associated with an independent YSO, while B217 has a "dumbbell" morphology, with only one embedded object known, located between the two clumps (see BM). Tamura et al. (1991) have recently presented a deep 2.2 μm image of the source (IRAS 04248+2612) at the center of the B217 complex, which reveals elongated emission perpendicular to the line between the clumps, perhaps suggesting that the B217 clumps are more closely related than the L1495 clumps. The position of the YSO in B217 is approximately coincident with highest (farthest from the mean) veloc-

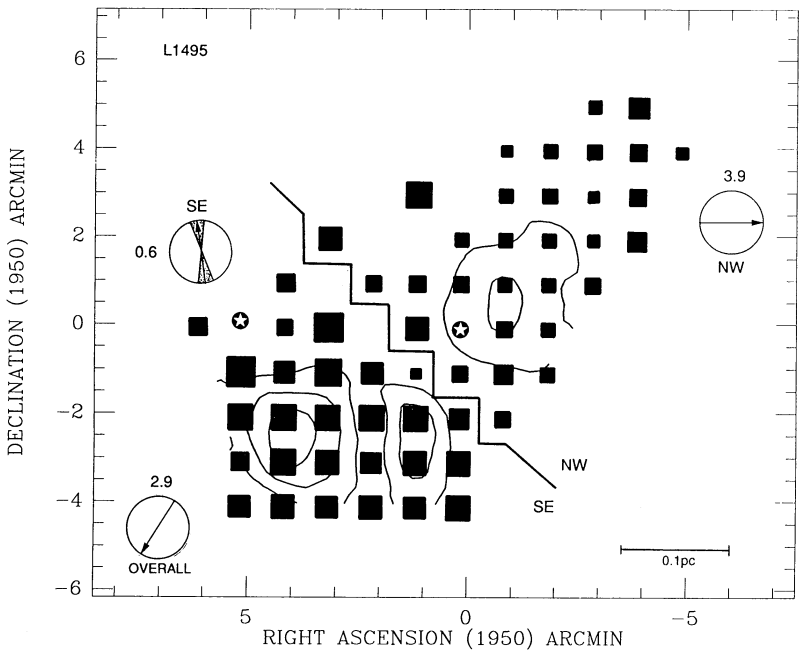

FIG. 4*a*

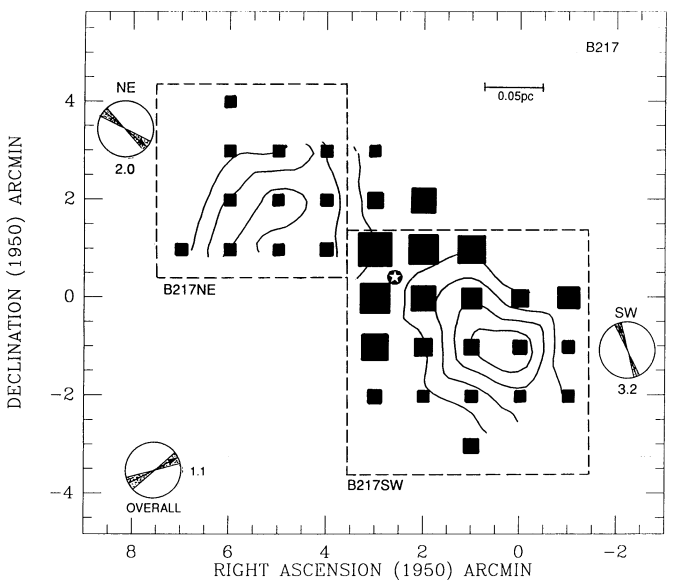

FIG. 4*b*

FIG. 4.—(*a*) NH_3 in L1495. Filled squares, contours, direction indicator, and star symbols have the same meanings as in Fig. 3. The (0, 0) position, velocity range, and contour levels are, respectively, ($04^h10^m49^s.3$, 28°03′58″), (6.00, 6.91 km s^{-1}), (0.2, 0.4, 0.6 K). Note that velocity gradients have been fitted to subsections (labeled "NW" and "SE") of the cloud, as well as to all the emission (indicator labeled "overall"). (*b*) NH_3 in B217. Filled squares, contours, direction indicator, and star symbols have the same meanings as in Fig. 3. The (0, 0) position, velocity range, and contour levels are, respectively, ($04^h24^m42^s.5$, 26°12′13″), (6.78, 7.43 km s^{-1}), (0.2, 0.4, 0.6, 0.8 K). Note that velocity gradients have been fitted to subsections ("NE" and "SW") of the cloud, as well as to all the emission (indicator labeled "overall").

ities observed, near the center of the map. This projected coincidence might suggest interaction between the YSO and the core, but more evidence is necessary before such a speculation can be supported.

3.5. *Comparisons among Neighboring Clouds: L1251*

The dense cores "L1251E" and "L1251A" are both located in the elongated dark cloud Lynds 1251. In projection, L1251E surrounds IRAS 22376+7455, and L1251A contains the much fainter *IRAS* source known as 22290+7458. We detect highly significant velocity gradients in both of these cores, but the gradient directions lie 79° apart from each other (i.e., virtually orthogonal). This fact suggests that these cores are not the result of a simple fragmentation process where a specific orientation of angular velocity is preserved over scales of several parsecs.

Using the observational techniques described in Goodman et al. (1990), Goodman, Bastien, & Myers (1993) have sparsely mapped the optical polarization of background starlight in the region of the L1251 dark cloud. The inferred plane-of-the-sky magnetic field direction is 49° east of north, with a small dispersion (11° standard deviation in 11 reliable measurements). Note that 49° is indistinguishable from −131° for a polarization measurement, where the "sign" of the plane-of-the-sky field is not known. Thus, neither L1251A ($\theta_{\hat{\omega}} = 13° \pm 8°$) or L1251E ($\theta_{\hat{\omega}} = -66° \pm 2°$) appears to have a rotation axis oriented near the direction of the magnetic field.

Sato & Fukui (1989) have mapped the L1251 dark cloud in

^{13}CO emission, and they detect outflow in ^{12}CO from the *IRAS* source associated with L1251E, and from IRAS 22343+7501, which is located in the region between the two dense cores. Only the outflow from IRAS 22343+7501 has been mapped (Sato & Fukui 1989), and it is oriented at about 38° east of north, which is similar (in projection) to the field direction of 49°. Balázs et al. (1992) detected Hα knots marking out what they believe to be an optical jet from the source, the direction of which agrees with the *large-scale* (Sato & Fukui) outflow. However, Schwartz, Gee, & Huang (1988) have also mapped a CO outflow from this source, with ~3 times the resolution of Sato & Fukui, and they find a direction of 150° east of north, very different from the large-scale flow. Therefore, in L1251, there is some similarity among the directions of the optical polarization vectors, a large-scale outflow, and an optical jet, but wide divergence in the directions of the individual core velocity gradients and the small-scale outflow.

When we use all the NH_3 data available, and fit a gradient to the L1251A and L1251E cores taken together, we find a gradient of 2.2 ± 0.1 km s^{-1} pc^{-1} at $-176\overset{\circ}{.}3 \pm 0\overset{\circ}{.}3$ east of north, and a mean velocity of -4.1 ± 0.3 km s^{-1}. Using VFIT on Sato & Fukui's (1989) ^{13}CO data for the L1251 dark cloud, we find a gradient of 0.43 ± 0.02 km s^{-1} pc^{-1} at $-176° \pm 1°$ east of north, and a mean velocity of -3.9 ± 0.3 km s^{-1}. Thus, despite the tremendous gap in the NH_3 data in the space between the two cores, and the difference in gradient direction from core to core, the direction of the component of solid-body rotation appears to be preserved from the dark cloud to the core densities—at the "dark cloud" (of order several pc) scale. This alignment of gradient directions in L1251 is an example of the preservation of gradient direction from one tracer to the next, discussed further in § 5.1).

3.6. *Kinematics of Cores within Clouds: A Detailed View of L43*

Lynds 43 is an elongated dark cloud (~1.7 × 0.3 pc) associated with at least two very young stars, RNO 90 and RNO 91 (Cohen 1980). The velocity structure of the dense gas associated with L43 (Fig. 5) exhibits a very clear almost west-east gradient near the peak of the NH_3 emission (near RNO 91), and a less obvious but still very significant gradient in the "ambient" NH_3 which points in a distinctly different direction.

Mathieu et al. (1988) analyze the morphology of the L43 region, and discuss velocity gradients in NH_3 and CS maps of the region near RNO 91 (the embedded T Tauri star IRAS 16316−1540). Pastor et al. (1993) present CS ($J = 1 \rightarrow 0$) and $C^{18}O$ ($J = 1 \rightarrow 0$) observations of the same region, and find velocities and gradients similar to those discussed by Mathieu et al. The analysis presented here includes the region of L43 studied by Mathieu et al. and Pastor et al., as well as the portion of the L43 dark cloud to the west of RNO 91, which produces very weak NH_3 emission and is more obviously associated with RNO 90 (IRAS 16312 − 1542).

By taking constant-declination cuts through NH_3 maps, Mathieu et al. (1988) found a velocity gradient which ranges from 0.4 to 3.5 km s^{-1} pc^{-1}, depending on where along the cut one calculates the slope of v_{LSR} as a function of position. Using only the data for the subregion of the L43/RNO 90 NH_3 complex discussed by Mathieu et al., our fitting routine calculates a gradient of 1.6 ± 0.2 km s^{-1} pc^{-1} along almost exactly a west-east direction ($88° \pm 11°$ east of north) representing an average value along the cut of Mathieu et al. (Note that "L43" in Tables 1 and 2 refers only to this core region, which is associated with RNO 91 and bounded approximately by the 0.25 K contour shown in Figure 5. "L43/RNO 90" refers to the entire region shown in Figure 5, which includes all of the NH_3 observed to be associated with RNO 90 *and* RNO 91.) If, however, all of the NH_3 data are included, the resulting gradient is 1.3 ± 0.1 km s^{-1} pc^{-1} at $130° \pm 6°$ east of north. Thus, the gradient in the "L43" core (associated with RNO 91) is about 40° different from the underlying "ambient" gradient, to within an uncertainty of less than ~10°. Indeed, even if all of the data associated with the "L43" core region are excluded, the remaining data still give a gradient of 1.1 ± 0.2 km s^{-1}

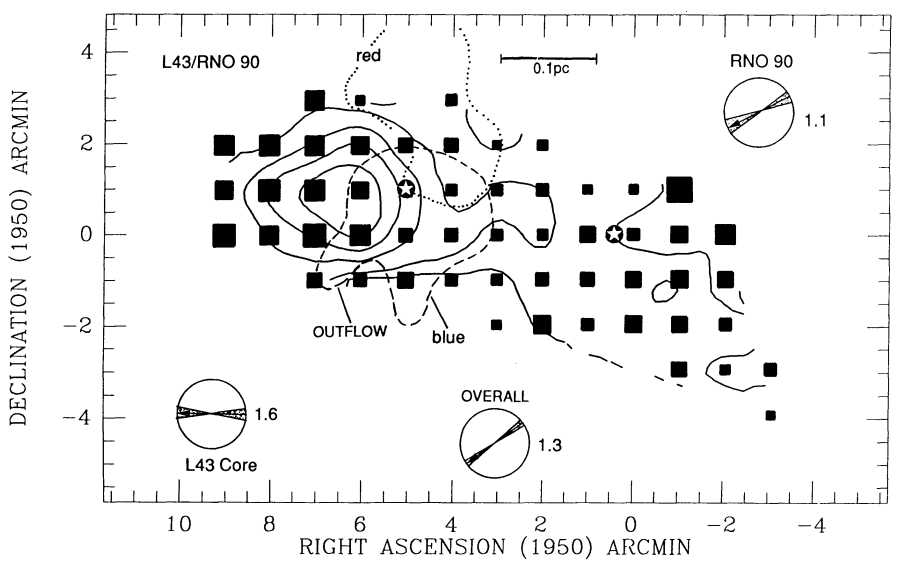

FIG. 5.—NH_3 in the L43/RNO 90 complex. Filled squares, contours, direction indicator, and star symbols have the same meanings as in Fig. 3. The (0, 0) position, velocity range, and contour levels are, respectively, ($16^h31^m18\overset{s}{.}5$, $-15°41'40''$), (0.19, 0.87 km s^{-1}), (0.15, 0.25, 0.50, 0.75, 1.00 K). Note that velocity gradients have been fitted to the core associated with RNO 91 (labeled "L43 core"), to the emission that does not include the "L43 core" (labeled "RNO 90"), and to all the emission (indicator labeled "overall"). The location of the outflow associated with RNO 91 in the L43 core is shown schematically (see Mathieu et al. 1988).

pc^{-1} at 124° ± 11° east of north, very similar to the gradient we find for the whole complex. Therefore, the L43 core velocity gradient appears distinct from that of its environs.

The L43 core is also distinct in maps of the spectral-line width of the NH_3 emission in the L43/RNO 90 complex. All of the line widths within the half-power contour around RNO 91 are within 0.05 km s^{-1} of the mean value, while the FWHM of the distribution of line widths for the entire complex is about 0.3 km s^{-1}, 6 times larger. (Near the edge of a map, fitting low signal-to-noise spectra can artificially produce large line widths, but the effect we observe is seen in higher signal-to-noise spectra as well.) Using CS and finer resolution NH_3 observations than those presented here, Mathieu et al. (1988) found larger line widths at positions coincident (in projection) with the CO outflow from IRAS 16316−1540 (RNO 91), and they interpreted the larger line widths as evidence for interaction of the outflow with the dense gas in L43. At the resolution of our maps, we cannot reliably identify evidence of larger line widths associated with the outflow.

Fuller (1989) fitted velocity gradients to CS ($J = 2 \rightarrow 1$) and $C^{18}O$ ($J = 1 \rightarrow 0$) spectral-line maps of L43. (We discuss in § 5.1 comparisons among NH_3, CS, and $C^{18}O$ gradients in several additional clouds also mapped by Fuller 1989.) Using the same fitting procedure described in this paper, Fuller finds a gradient of 0.69 ± 0.06 km s^{-1} pc^{-1} at 102° ± 9° east of north in the CS map, and 0.54 ± 0.09 km s^{-1} pc^{-1} at 86° ± 26° east of north in the $C^{18}O$. Although the extent of the NH_3 map shown in Figure 5 is larger than that of the $C^{18}O$ and CS maps, the FWHM contours of the $C^{18}O$, CS, and NH_3 maps are progressively smaller, implying that they are sampling progressively denser portions of a cloud whose density decreases monotonically outward (see Fig. 4 of Myers et al. 1991). If this is the case, then we might expect the gradient directions measured in $C^{18}O$ and CS to lie between the NH_3 core direction (88° ± 11°) and the larger scale complex-wide gradient direction (130° ± 6°), which appears potentially to be the case.

3.7. NH_3 "*Outflow*" *in L1551*

In a spectral-line map with sufficient spatial and velocity resolution, useful information is often contained in a map of ($v_{LSR} - v_{FIT}$), where v_{FIT} is the velocity predicted by fitting a first-order gradient (eq. [1]). These fit residuals can reveal higher order structure in the velocity field which is otherwise masked by solid-body rotation. For most of the cores discussed in this paper, there are not enough points in the map to warrant analysis of the residuals. So, in order to illustrate the utility of analyzing fit residuals, we present a new analysis of Menten & Walmsley's (1985, hereafter MW) high-resolution NH_3 map of L1551, which includes 47 measurements of v_{LSR}.

MW used the 100 m Effelsberg telescope to map NH_3 (J, K) = (1, 1) emission in the dense gas associated with the protostellar source L1551 IRS 5. Their spatial resolution was 40″, and their map is oversampled, with 20″ spacing in both spatial directions. (Most of the maps presented in BM are much coarser, with 1′ spacing and a 90″ beam.) The velocity resolution in the MW observations was 0.16 km s^{-1}, but the accuracy with which v_{LSR} is known for a given spectrum is generally ∼0.02 km s^{-1}, after detailed fitting of the multi-component line profiles.

The velocity field in the L1551 NH_3 map is shown in Figure 6*a*. MW fitted a velocity gradient to this data set, and our fit is consistent with theirs. The linear fit (eq. [1]) yields a well-defined gradient of 4.03 ± 0.09 km s^{-1} pc^{-1}, corresponding to solid-body rotation with $\theta_{sb} = 3\overset{\circ}{.}0 \pm 0\overset{\circ}{.}9$. (Note that L1551 is not listed in Tables 1 and 2, since its solid-body rotation was already discussed by MW.) MW note that "the dynamical situation [in L1551] is too complex to be described by a simple rotational model," and they further suggest that velocity versus position cuts through the data show a second gradient along the southwest-northwest direction, whose sign is consistent with the observed outflow from IRS 5. MW claim that the data show "marginal evidence for ... some slight interaction with the outflow."

Figure 6*b* shows a contour plot of the residuals, v_{LSR} versus v_{FIT}, resulting from subtracting the first-order gradient (i.e., solid-body rotation) from the MW data. Two peaks are apparent, one spanning the velocity range from about 0.04 to 0.08 km s^{-1} and the other from −0.04 to −0.10 km s^{-1}, with respect to the local value of v_{FIT}. These two peaks appear to be significant evidence for interaction of the outflow from the YSO IRS 5 with the surrounding dense gas. The evidence here is "significant," rather than "marginal" as in MW, because here the residuals are imaged in two dimensions and show spatial structure consistent with outflow interaction.

The bipolar "CO" outflow associated with IRS 5, first discovered by Snell, Loren, & Plambeck (1980; see also Moriarty-Schieven & Snell 1988), is oriented at a position angle of approximately 57° east of north, with an opening angle of $\lesssim$70°. Evidence for the same outflow has also been found in the high-velocity wings of OH lines seen in absorption (Mirabel et al. 1985). The NH_3 "lobes" in Figure 6*b* are oriented along approximately the same direction as the CO and OH lobes, and the sign of the velocity shifts agrees with the CO and OH results. Thus, the motions evident in Figure 6*b* are probably related to the outflow rather than to a second-order rotation.

The total span of velocity in the "outflow" that we find by analyzing the residuals is only ∼0.2 km s^{-1}, over about 1′, but this corresponds to an implied outflow gradient (i.e., roughly southwest-northeast) of 4.6 km s^{-1} pc^{-1}, which is similar in magnitude to the core's first-order rotational gradient (i.e., almost south-north), at an assumed distance of 150 pc.

If the NH_3 lobes represent the action of the wind emanating from IRS 5, the expected velocity of a lobe can be estimated, based simply on the transfer of momentum from the wind to the dense gas. Assuming that a neutral atomic wind with a typical density of 10 cm^{-3} and a velocity of 190 km s^{-1} is driving the observed CO outflow (Lizano et al. 1988), then conservation of momentum within a constant volume (i.e., density × velocity = constant) predicts a typical lobe velocity of 0.06 km s^{-1} for gas with a density of $10^{4.5}$ cm^{-3}, representative of the NH_3 emission in L1551. This predicted velocity is similar to the observed lobe velocities, supporting the idea that the NH_3 velocity field arises in part from interaction of a wind from IRS 5 with the dense gas.

Another case of interaction between outflow and dense gas has been documented, in the Cepheus A cloud, where Torrelles et al. (1987) detect outflow in both the CS $J = 1 \rightarrow 0$ transition and the NH_3 (J, K) = (1, 1) transition. They too find evidence for interaction of the outflow with the dense gas by "removing" the effects of solid-body rotation. They plot spatial-velocity diagrams along cuts perpendicular to the deduced solid-body rotation axis, and find structure indicative of an outflow. Their technique does not allow for a detailed comparison of outflow position angle, but, by comparing the

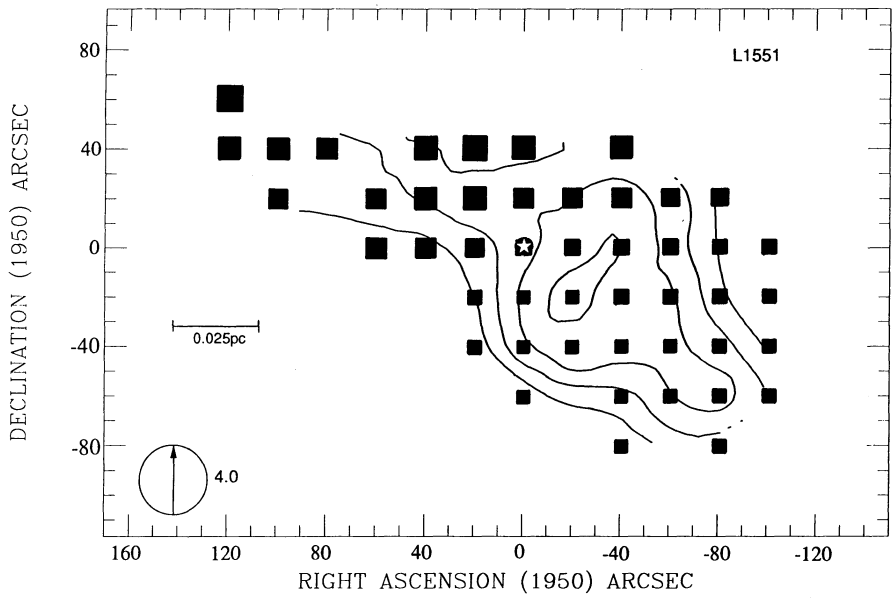

FIG. 6a

FIG. 6.—(*a*) NH_3 $(J, K) = (1, 1)$ emission in L1551 (Menten & Walmsley 1985). Filled squares, direction indicator, and star symbols have the same meanings as in Fig. 3. (The star here shows the position of L1551 IRS 5.) Contours map the peak main-beam brightness temperature. The (0, 0) position, velocity range, and contour levels are, respectively, ($04^h28^m40^s$, 18°01′52″), (6.21, 6.63 km s^{-1}), (3, 4, 5, 6 K). (*b*) Velocity residuals ($v_{LSR} - v_{FIT}$) in the NH_3 map of L1551 (Menten & Walmsley 1985) after the gradient indicated in (*a*) is removed. The single dark contour shows the 4 K brightness temperature contour. Lighter dashed contours show velocities of 0.04, 0.06, and 0.08 km s^{-1} for the redshifted gas, and the lighter solid contours show velocities of −0.04, −0.06, −0.08, and −0.10 km s^{-1} for the blueshifted gas, where these velocities are measured with respect to the local value of v_{FIT}. The map is superposed on the ^{12}CO map of the outflow from IRS 5, which is illustrated with open dashed and solid contours, showing the red- and blueshifted lobes, respectively (from Snell, Loren, & Plambeck 1980).

momentum in the low-density outflow (mapped in ^{12}CO by Ho, Moran, & Rodríguez 1982) with that in the denser gas traced by CS, Torrelles et al. demonstrate that there is rough momentum conservation in the outflow.

4. RELATIONS BETWEEN GRADIENTS AND CLOUD PROPERTIES

4.1. *Gradient Direction and Core Elongation*

If core velocity gradients resulted from energetically significant rotation, then one could expect cores to be flattened along $\hat{\omega}$, in response to centrifugal stress. If this were the case, $\hat{\omega}$ would be approximately perpendicular to the long axis of a core. Furthermore, if cores were rotationally flattened, they would be oblate, which, for many cores, is unlikely (Myers et al. 1991). Alternatively, if rotation does not control cloud dynamics, but $\hat{\omega}$ is determined by another influence (e.g., a magnetic field) which also determines the orientation of the cloud, one might still expect to find systematic orientation of $\hat{\omega}$ with respect to a cloud's long axis. Heyer et al. (1987) have suggested that dark cloud elongation, field direction, and rotation axes are indeed related in this way in the Taurus dark cloud complex. Yet the results of Goodman et al. (1990) suggest that dark cloud elongation and field direction are *not* well correlated, especially when one considers the deprojection of observed plane-of-the-sky angles into real space. And the results below suggest that it is not likely that $\hat{\omega}$ is correlated with large-scale field direction, either.

Figure 7 shows the distribution of the difference between $\theta_{\mathcal{G}}$ and the position angle of the long axis of a core. The distribution is consistent with a completely random orientation of $\hat{\omega}$ with respect to core orientation. Therefore, we conclude that the observed gradients have no causal relation with core elongation, on the size scale of 10^{17} cm.

In addition, the orientation of gradients within a complex appears to be random. The gradient direction for the 15 Taurus cores listed in Tables 1 and 2 have an apparently unpeaked distribution of $\theta_{\mathcal{G}}$, spanning the entire range of possible orientations. This confirms Goldsmith & Sernyak's (1984) conclusion that the gradient directions in Taurus appear uncorrelated. These results are contrary to the idea that core velocity gradients are identifiable descendants of galactic rotation. It is also unlikely that $\hat{\omega}$ is controlled by the large-scale magnetic field, which exhibits far less dispersion in Taurus (Goodman et al. 1990) than does the distribution of $\theta_{\hat{\omega}}$. Instead, it appears that more stochastic processes, such as fragmentation, collisions, and nonuniform magnetic fields, are responsible for the orientation of the observed gradients.

4.2. *Gradient Magnitude and Core Shape*

Figure 8 shows $\mathcal{G}$ as a function of core axial ratio, and is intended to answer the question "do 'rounder' objects spin faster?" A formal fit to this graph finds no detectable correlation. Since we find no correlations in this data set among core elongation and the direction of rotation, and there is no evidence for rotational flattening and it is likely that cores are prolate, it is not surprising that a core's axial ratio and its rotational velocity are unrelated.

4.3. *Gradient Properties and the Presence of a YSO*

Figure 9 shows the distributions of gradient magnitudes for cores with and without stars. A core "with" a star is defined as having at least one YSO within 1 map FWHM diameter of the

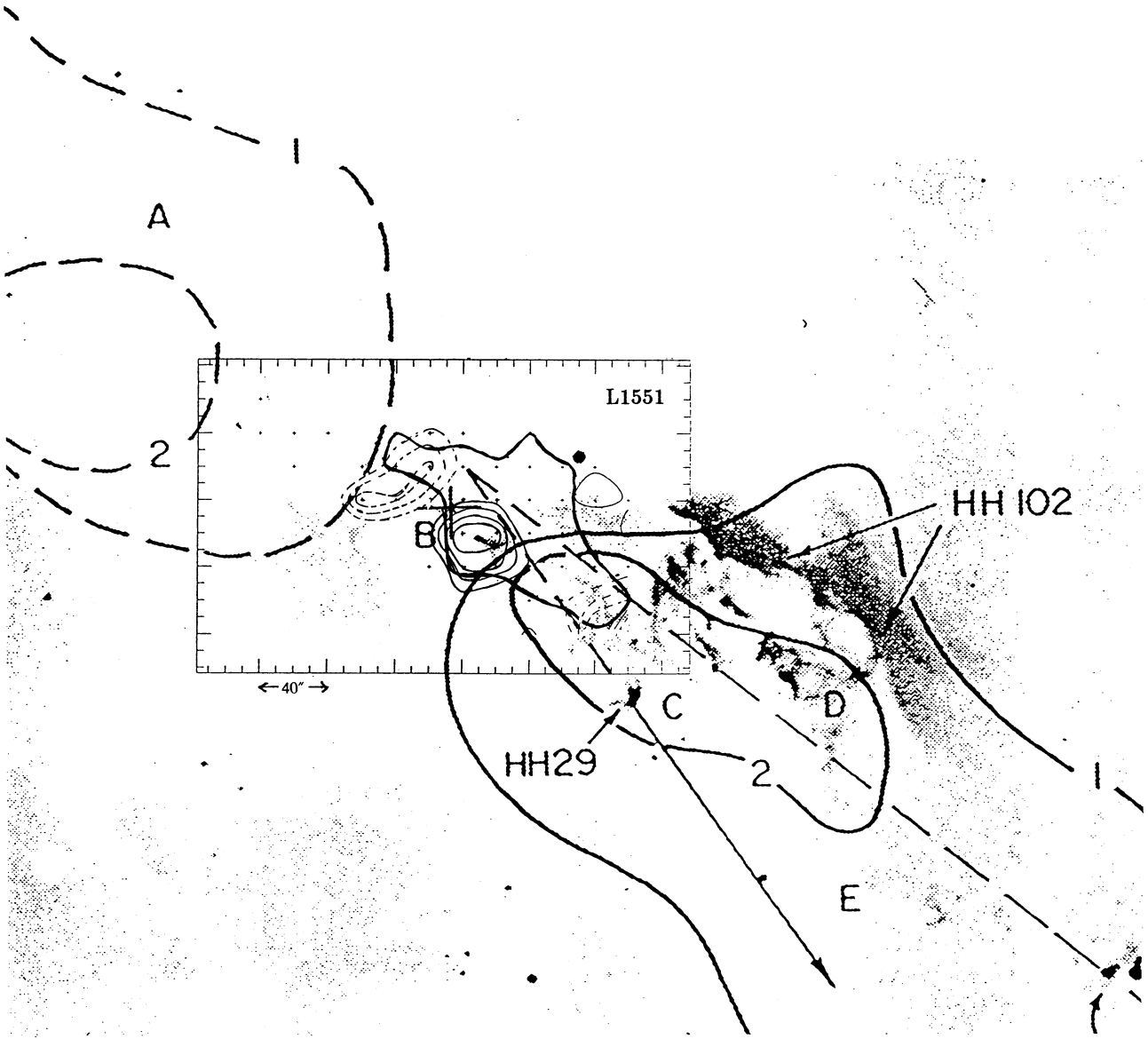

FIG. 6*b*

map peak. The distributions are statistically indistinguishable. Gradient magnitude seems unrelated to the presence of a star, unlike line width, which has been shown to be larger, on average, for cores with stars (BM).

We find no correlation between the direction of the gradient and the direction of offset between the peak of the NH_3 map and the nearest embedded source. And we find no correlation between the magnitude, and/or the significance, of the gradient in a core and the quantity D/R, defined (in BM) as the distance from the core peak to the nearest YSO divided by the FWHM core size. It appears that the relation between the position of the peak of the NH_3 map and the position of the nearest YSO are not related to the velocity gradients we measure in NH_3 maps of dense cores.

5. COMPARISON WITH GRADIENTS FOUND USING OTHER TRACERS

5.1. *Comparison with* CS *and* $C^{18}O$ *Results*

Fuller (1989) mapped 14 of the NH_3 cores discussed in this paper in the $J = 2 \rightarrow 1$ CS transition and the $J = 1 \rightarrow 0$ transition of $C^{18}O$. The spatial resolution and spectral resolution of his observations are typically as high as, or higher than, those of the NH_3 observations. Using the same fitting routine discussed in § 2.1, Fuller has calculated velocity gradients for all the clouds he observed.

Figures 10*a* and 10*b* show correlations between the NH_3 and CS and the NH_3 and $C^{18}O$ gradient directions. Least-squares fits to these correlations give slopes of 0.94 ± 0.09 and

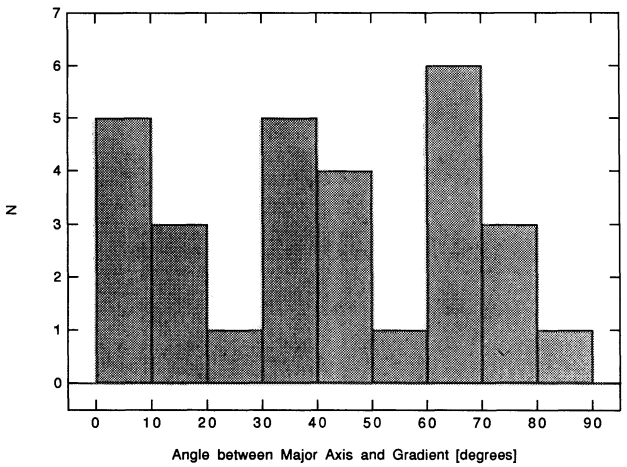

FIG. 7.—Distribution of angles between the observed long axis of a core and the direction of its velocity gradient. All 29 cores where we can determine this angle are included.

0.7 ± 0.2, respectively. The tight correlation of gradient directions, especially between the CS and NH_3 results, indicates that these tracers are indeed mapping out a real physical entity. This point of view is also supported by the good correlation of elongation position angles for maps of the same core in different tracers (see Myers et al. 1991).

The uncertainties in the magnitude of the NH_3 gradients are typically ~ 0.3 km s^{-1} pc^{-1}, which is large enough compared with the range of gradients observed that little correlation with the magnitude of the CS or $C^{18}O$ gradients is expected or seen. The errors in the CS and $C^{18}O$ gradients are typically smaller, and one *can* see a correlation in their magnitudes, which will be discussed in detail in Fuller, Goodman, & Myers (1993).

5.2. *Comparison with* ^{13}CO *Results*

Arquilla & Goldsmith (1986, hereafter AG86) have carried out a thorough analysis of eight molecular clouds, six of which had been reported in the literature to be rotating (see also Goldsmith & Arquilla 1985). Using a fitting procedure different from ours on spectral-line maps of the $J = 1 \rightarrow 0$ transition of ^{13}CO, they find evidence for true solid-body rotation in only three of six clouds previously claimed to be rotating. The authors conclude that "rapid rotation in dark clouds may be much rarer than previously suspected." However, the rotational energy associated with the clouds they do find to be rotating is dynamically significant (see § 6). In the clouds found *not* to be rotating, AG86 attribute previous claims of rotation to confusion between rotation and other kinetic processes, including gas flow and clump motions.

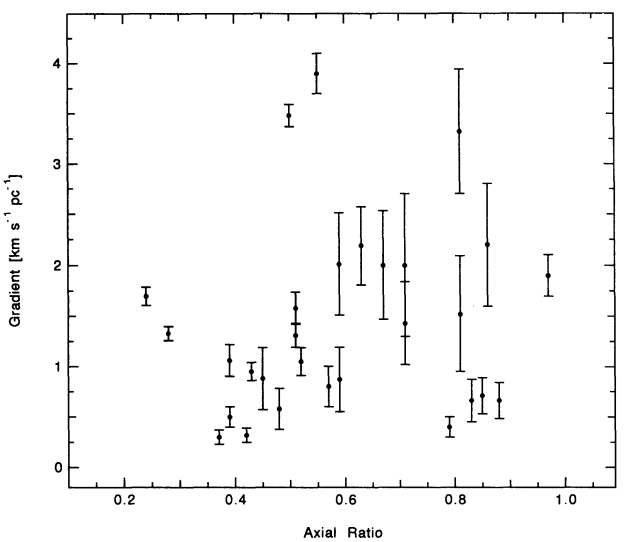

FIG. 8.—Velocity gradient as a function of core axial ratio [= (minimum diameter of FWHM contour)/(maximum diameter of FWHM contour)].

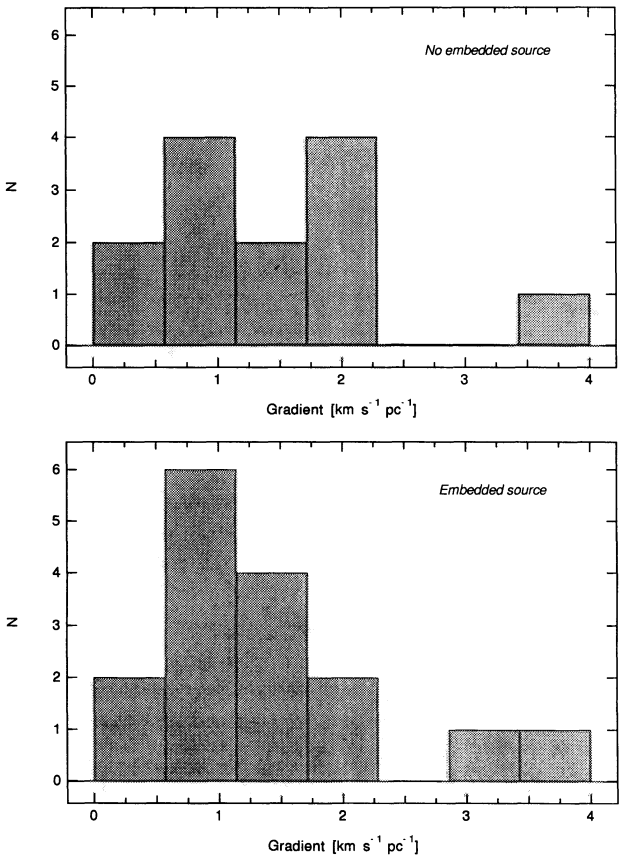

FIG. 9.—Distribution of gradient magnitude for cores with and without an embedded source less than one core diameter from the NH_3 map peak.

B361 is the only cloud analyzed both in this paper and by AG86. Arquilla & Goldsmith (1985, hereafter AG85) find evidence for solid-body rotation of a "core" region at 3.3 km s^{-1} pc^{-1}, and differential rotation of an "envelope" region, with $\omega(r) \propto r^{-1}$. AG86 find the direction of the "kinematic axis" (equivalent in our notation to $\theta_{\hat{\omega}}$) in B361 to be $42° \pm 9°$ east of north. The gradient we find in NH_3 for B361 is oriented with $\theta_{\hat{\omega}} = 58° \pm 12°$, consistent with the AG86 result, and lending support to their proposal of a rigidly rotating core.

The magnitude of the NH_3 gradient is 0.7 ± 0.2 km s^{-1} pc^{-1} in B361, which is 5 times smaller than the gradient derived from ^{13}CO data by AG86. Both estimates assume that the distance to the cloud is 350 pc, although this distance estimate is very uncertain (Arquilla 1984). AG's large gradient leads them to find a very large rotational energy in B361 (in comparison to its gravitational energy), an important problem which we discuss in § 6.2 below.

The results of AG86 indicate that large maps made with probes which trace a relatively low critical density give compli-

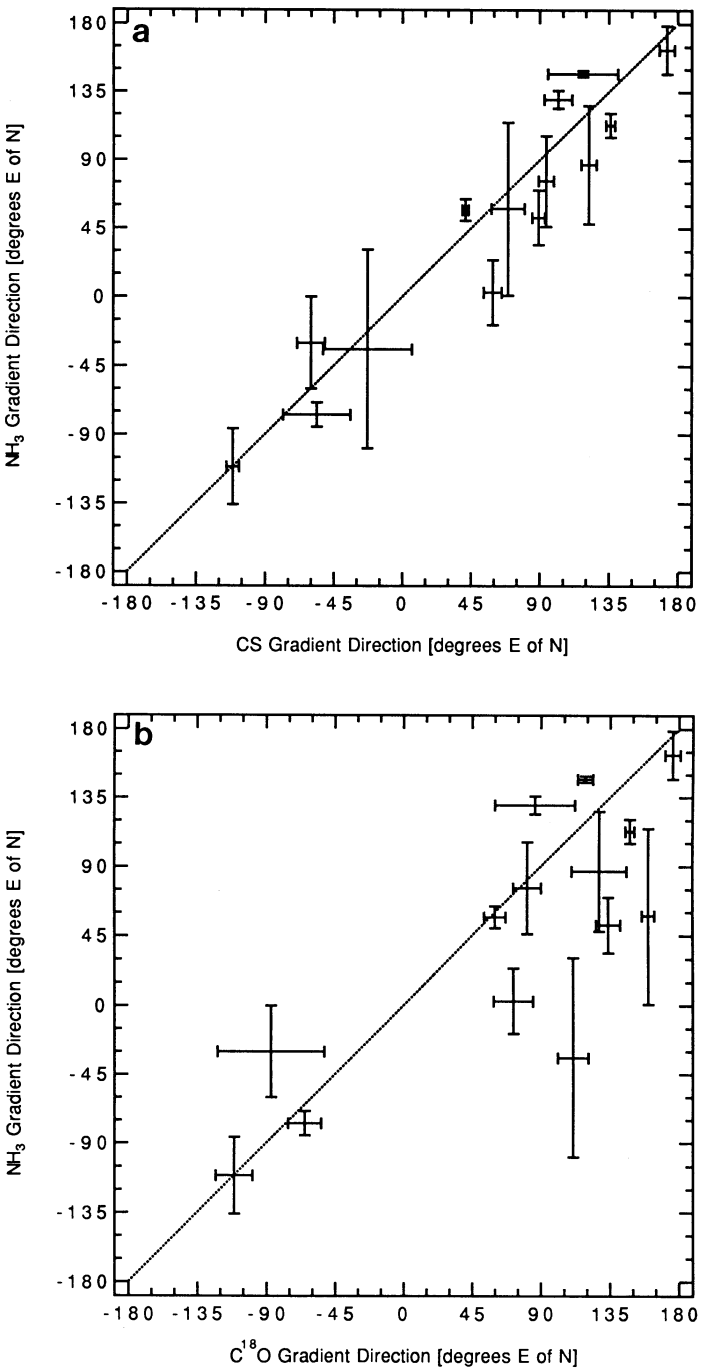

FIG. 10.—Comparisons of gradient direction among several tracers. (*a*) Comparison of velocity gradient fits to NH_3 maps with fits to CS maps; (*b*) comparison for NH_3 and $C^{18}O$. In both figures, the slope of the reference (*dotted*) line is 1.

cated velocity fields which can mimic solid-body rotation. In L1495 a comparison of NH_3 and $C^{18}O$ data illustrates this effect. There the lower density tracer, $C^{18}O$, gives a gradient dominated by clump-clump motion, and the higher density tracer, NH_3 reveals small clumps and can give distinct gradients for each clump if each is fitted alone, *or* a gradient consistent with the $C^{18}O$ if fitted as one map (§ 3.4).

6. DISCUSSION: IMPLICATIONS FOR MODELS OF DENSE CORES

6.1. *Determination of* β

The parameter β, defined as the ratio of rotational kinetic energy to gravitational energy, can be used to quantify the dynamical role of rotation in a cloud. We write

$$\beta = \frac{(1/2)I\omega^2}{qGM^2/R} = \frac{1}{2}\frac{p}{q}\frac{\omega^2 R^3}{GM}, \tag{5}$$

where, for the particular shape and density distribution of the cloud, the moment of inertia is given by $I = pMR^2$, and q is defined such that qGM^2/R represents the gravitational potential energy of the mass M within a radius R. For a uniform density sphere, $q = \frac{3}{5}$ and $p = \frac{2}{5}$, so $p/q = \frac{2}{3}$. For a sphere with an r^{-2} density profile, $p/q = 0.22$, which reduces β, for fixed M, ω, and R, by a factor of 3 compared with the uniform density case.

For a sphere with constant density ρ_0, equation (5) gives

$$\beta = \frac{1}{4\pi G\rho_0}\omega^2 = \frac{1}{4\pi G\rho_0}\frac{\mathcal{G}^2}{\sin^2 i}. \tag{6}$$

Figure 11 presents the distribution of β, based on the NH_3 data, for all the cores in Table 1 where a reliable calculation of β is possible, with the assumptions of uniform density and $\sin i = 1$. The density values used in calculating β are taken from the references listed in Table 1.

For a distribution where any orientation of $\hat{\omega}$ (in three dimensions) is equally likely, $\langle \mathcal{G}^2/\sin^2 i\rangle = (3/2)\langle \mathcal{G}^2\rangle$ (see Chandrasekhar & Münch 1950; Tassoul 1978). So, if an average value of β is derived from an unbiased random distribution of gradient orientations, it should be multiplied by 3/2 to account for projection effects. In the present analysis,

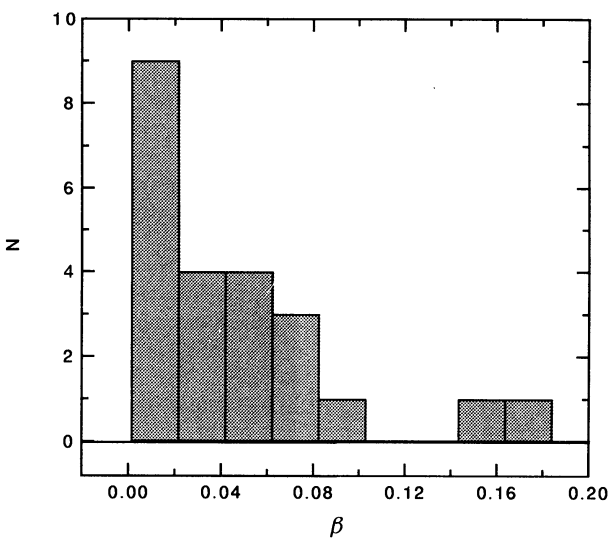

FIG. 11.—Distribution of β, shown for the 23 cores where enough information is available to calculate β *without* assuming virial equilibrium (i.e., the estimate of gravitational energy is based on the measured cloud size and a derived volume *density*, not on line width). Note that the value of $\beta = 1.4$ for L1495NW is not included in this distribution; this seemingly discrepant value is discussed in the text (§ 6.2).

upper limits have been excluded, so the distribution in Figure 11 will be biased toward higher β, calling for a reduction in this "typical" deprojection correction factor. The product of these factors is of order unity, so applying an exact correction would not change our main results.

6.2. *Numerical Values of* β

With the exception of L1495NW, which ostensibly has $\beta = 1.4$, all clouds we studied have $\beta \leq 0.18$, and most clouds have $\beta \leq 0.05$.

L1495NW seems a special case. It has a significant gradient, 3.9 ± 0.2 km s^{-1} pc^{-1}, and it is within a factor of 2 of virial equilibrium [i.e., $GM/5R = \Delta v^2/(8 \ln 2)$; see § 6.4 below]. Since this large gradient in a small cloud implies an unusually large amount of rotational energy, we have carefully analyzed the residuals for this fit. There is structure in the residuals, but none which would imply that the large gradient in L1495NW is spurious.

The typical values of β presented here (Table 2) are quite low in comparison with the values ($0.4 \lesssim \beta \lesssim 1.2$) derived from ^{13}CO data by AG86. In fact, AG86 note that their estimates of β seem high, and they suggest that this phenomenon is partially caused by the contamination of their determination of ω by low-density cloud envelopes which contain substantial amounts of rotational energy. We also find that large values of β can often be attributed to a size and/or mass mismatch between the region giving rise to the derived ω and the region for which β is calculated.

Equation (5) shows that if M increases more slowly than R^3, which is true in any cloud where the power-law index of the density profile is negative, then β becomes a monotonically increasing function of R, for constant ω, p, and q. For the dark clouds studied by AG86, this type of density profile is always applicable, at least to the so-called envelopes of the clouds, as traced by ^{13}CO. Therefore, an overestimate of R, for a given ω, will produce too large a value of β. An underestimate of M, for a given R, will also have the same effect.

As an example, we can again consider B361 (see § 5.2). The value of β for B361 listed in AG86, based on ^{13}CO data, is 0.9. However, this value is not self-consistent, in that it uses mass and size values relevant to the cloud "envelope" and a value for ω which AG86 derive for the rigidly rotating cloud "core" of B361. If instead the angular velocity (1.1×10^{-13} s^{-1}), size (0.17 pc), and volume density (4.5×10^{-20} g cm^{-3}) of the rigidity rotating core region (AG85) are used together, then substituting in equation (5) gives $\beta = 0.3$. Using exclusively NH_3 data, which give a FWHM cloud size of 0.32 pc and a mass of about 50 $M_\odot$, we find $\beta = 0.03$. The mass of the "core" identified in ^{13}CO is only about 12 $M_\odot$, so it is not surprising that the NH_3-derived and the ^{13}CO-derived core gradients differ substantially. In fact, if one substitutes the NH_3-derived gradient and the AG85 core size and mass, one finds $\beta = 0.01$, almost 100 times smaller than the value quoted in AG86. We conclude that *gradients determined using low-density tracers can be contaminated by gas at the size scale most populated by that tracer, and thus can give inappropriate estimates of* β, a result also suggested by the analysis in AG86.

6.3. *Implications of* $\beta \lesssim 0.1$

In general, if β is very large, a gas cloud can become stable against gravitational instabilities, potentially inhibiting fragmentation and star formation (cf. Goldreich & Lynden-Bell 1965; Nakano 1984; Larson 1985). And if β is very small, a cloud will never have enough rotational energy to experience instabilities driven by rotation alone, such as fission.

Several theoretical efforts have predicted specific values of β to be associated with specific events, such as the formation of nonaxisymmetric instabilities (e.g., bars, fission) or axisymmetric instabilities (e.g., rings). Direct comparison of these "critical" values of β with the results in this paper is often possible, but not prudent, since the models may assume cloud structure very different from what is observed on the $\sim 10^{17}$ cm size scale, as probed by NH_3 mapping. For example, many of the models predict cloud flattening perpendicular to the rotation axis, due to centrifugal stress, which, as discussed in § 4.1, is not typically observed. In addition, we find no evidence for a correlation of $\theta_{\hat{\omega}}$ with cloud orientation at this size scale (Fig. 7) and no significant correlation of angular velocity with axial ratio (Fig. 8). In many theories of rotating clouds, both of these correlations are either assumed, expected, or predicted.

Nonetheless, it is interesting to at least note the theoretical implications of certain values of β. Kiguchi et al. (1987), in an extension of the pioneering work of Stahler (1983a, b), have modeled rotation in isothermal clouds under the assumption that the clouds are axisymmetric and embedded in a stationary external medium. The effects of magnetic fields are not included in the Kiguchi et al. models (see Tomisaka et al. 1988a, b, 1989, 1990 for models which include rotation and magnetic fields). They find that at $\beta \geq 0.44$, no stable equilibrium solutions are possible, because the cloud becomes unstable to ring formation. However (as noted in Kiguchi et al.) nonaxisymmetric instabilities, such as the formation of a dynamical bar in a Maclaurin spheroid, are predicted (e.g., Chandrasekhar 1969; Tassoul 1978) to occur at a lower value, $\beta = 0.27$. And Hachisu, Tohline, & Eriguchi (1987) find that when one considers a compressible, centrally condensed gas cloud, rather than incompressible Maclaurin spheroid, Jeans-type nonaxisymmetric dynamical instabilities occur for $\beta \gtrsim 0.14$ rather than for $\beta \gtrsim 0.27$.

Regardless of the exact definition of "low," low β can inhibit fragmentation due to rotationally driven instabilities in molecular clouds. Boss (1988) estimates that in order for clouds to be able to fission due to rotation alone, β must be greater than 0.16. Since the typical value of β found in star-forming cores is much less than 0.16 (see § 6.2), Boss and others conclude that the fission instability is not prevalent and that binary stars likely do not form as a result of the fission of cloud cores. (This result is similar to the conclusion of Hachisu et al. 1987 that dynamical nonaxisymmetric instabilities only occur at $\beta \gtrsim 0.14$.) Instead, more complex "fragmentation" processes, involving gravitational and magnetic instabilities, must be prevalent (cf. Larson 1985; Bonnell & Bastien 1991; Bastien et al. 1991; Arcoragi et al. 1991; Bonnell et al. 1991).

It is also possible to set $\beta = 0$ in a cloud model which otherwise would include rotation, and still obtain realistic results. Tomisaka (1991; see also Tomisaka et al. 1988a, b, 1989, 1990) finds that after including the effects of the toroidal magnetic field, even if $\beta = 0$, realistic cloud models can still be produced. However, when radiative transfer is considered, if $\beta = 0$, opacity effects can permanently inhibit star formation. So, given that cores do form stars, there must be some nonzero rotation in cloud cores (Boss 1988).

6.4. *Relationship between* $\mathcal{G}R$ *and* Δv

It is well known (Larson 1981; Myers 1983; Myers & Goodman 1988, hereafter MG) that most self-gravitating dense

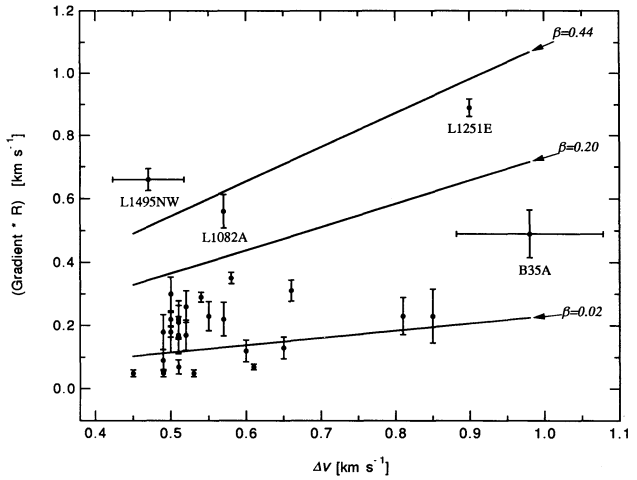

FIG. 12.—$\mathcal{G}R$, shown as a function of Δv, for a particle with mean mass. Vertical error bars are based only on the error in the fitted gradient, which is assumed to dominate errors in R. The error in Δv is typically 10%, and two representative error bars are shown. Lines of constant $\beta_{vir} = 0.02$, 0.20, and 0.44, calculated *with* the assumption of virial equilibrium (see text), are indicated. Cores for which this figure imply particularly high values of β_{vir} are labeled by name.

cores are close to virial equilibrium, i.e.,

$$3\sigma^2 \approx \frac{qGM}{R}, \tag{7}$$

where the one-dimensional velocity dispersion, σ, for a particle of average mass (2.33 amu) is related to the FWHM line width, Δv, by $\sigma = \Delta v/\sqrt{8 \ln 2}$.[3] Using equation (7), we can define β for a core in virial equilibrium as

$$\beta_{vir} = 0.92p\left(\frac{\mathcal{G}R}{\Delta v}\right)^2. \tag{8}$$

Therefore, straight lines with slope $1.04p^{-1/2}\beta_{vir}^{1/2}$ on a plot of $\mathcal{G}R$ as a function of Δv (Fig. 12) illustrate different values of β_{vir} (assuming $\sin i = 1$).

Figure 12 shows that clouds usually have gradients corresponding to less than a line width's worth of velocity shift across the cloud, and that normally the gradient is much smaller. Furthermore, Figure 12 shows that the data are best bracketed by $0 < \beta_{vir} < 0.2$, with 0.02 being a representative value. (It is assumed that $p = \frac{2}{5}$, appropriate for a constant-density sphere, in calculating the slopes shown in Figure 12.) Note that while Figure 11 is based on density measurements and plots β, and Figure 12 is based on line-width measurements and shows β_{vir}, both figures imply the same basic distribution of "β." This agreement indicates that the assumption of virial equilibrium is justified for these clouds, as is also indicated by Figure 6 of Myers et al. (1991). In a few individual cores (e.g., L1082A), there are significant discrepancies between β and β_{vir}. We attribute these discrepancies to measurement uncertainties in density, line-width, and cloud-size values, and to the possibility that not every cloud is near equilibrium.

[3] We calculate Δv for an "average particle" by subtracting, in quadrature, the NH_3 thermal line width from the observed line width, and adding back (in quadrature) the thermal line width of a particle with mass 2.33 amu (see Myers 1983 and MG). The values of Δv listed in Table 1 refer to such an average particle; they typically exceed the observed NH_3 line width by a factor of 2 or 3 (see BM for a table of observed NH_3 line widths and kinetic temperatures).

Figure 12 also indicates that the nonthermal broadening of spectral lines (i.e., the nonthermal energy observed in molecular clouds) cannot be prominantly due to rotation. If this were the case, we would expect to see a good correlation between $\mathcal{G}R$ and Δv, rather than many possible values of $\mathcal{G}R$ for a given Δv, as are observed. Rotation, even when it is present at easily detectable levels, does not significantly contribute to the observed line width. For example, if $\mathcal{G} = 1$ km s^{-1} pc^{-1}, then, for a cloud at 200 pc, a 1′ beam would give 0.06 km s^{-1} line broadening due to rotation—a very small fraction of 0.3 km s^{-1}, the typical NH_3 FWHM line width (see Table 1).

In simulations of rotating isothermal clouds, Kiguchi et al. (1987) find that the rotational speed, $v_\phi \approx \mathcal{G}R$ (assuming $\sin i = 1$), is at maximum about 2 to 3 times the sound speed in the core gas. Therefore, if the line widths observed in NH_3 cores are primarily thermal, the rotational speed should be less than about 0.4–0.6 km s^{-1}, as is evident in Figure 12.

6.5. *Dependence of ω and J/M on Cloud Size*

Using the type of virial equilibrium analysis discussed above (eq. [7]), and neglecting thermal contributions to the line width, one can deduce a scaling relation between line width and cloud size where $\Delta v \propto R^{0.5}$ (see Larson 1981; MG). In an empirical analysis, Larson (1981) found $\Delta v = 2.6R^{0.4}$, where Δv is in kilometers per second and R is in parsecs. Since Larson's work, several other similar scaling laws have been derived, both empirically and analytically (see MG and references therein). For cores where thermal line width is not negligible, the exponent in the size dependence of Δv is between 0 (purely thermal line width) and $\frac{1}{2}$ (negligible thermal line width). We continue to use $\frac{1}{2}$ in this discussion, despite the potential inaccuracy, so that our analysis can be applied to (the vast majority of) clouds where thermal line width is indeed negligible, and where a correlation of $\mathcal{G}$ with cloud size is apparent (see Goldsmith & Arquilla 1985).

In Figure 13*a* we plot $\mathcal{G}$ as a function of cloud size. We find that, in an unweighted least-squares fit,[4]

$$\mathcal{G} = 10^{-0.3\pm0.2}R^{-0.4\pm0.2}, \tag{9}$$

where $\mathcal{G}$ is in kilometers per second per parsec and R is in parsecs. In virial equilibrium, equation (8) and the relation $\Delta v \propto R^{\sim 0.5}$ apply, and their combination predicts that $\mathcal{G} \propto R^{-0.5}$, if β_{vir} is roughly constant. Figure 13*b* shows that β *is* roughly independent of R (i.e., ~constant), so we should expect to see a (rough) correlation like the one in equation (9). If we take a typical value of $\beta = 0.02$, assuming $\sin i = 1$, equations (8) and (9) imply a line width scaling law where

$$\Delta v = 10^{0.3\pm0.2}R^{0.6\pm0.2}, \tag{10}$$

using the same units as above. The coefficient and exponent in this statement of virial equilibrium are extremely similar to Larson's original fit and those derived since. The agreement is perhaps surprising, given the large amount of scatter in the correlation of gradient with size (Fig. 13*a*), which is due primarily to the large scatter in β (Fig. 13*b*).

We can also plot the specific angular momentum J/M, where $J = I\omega$, as a function of R (Fig. 13*c*). But, given equation (9) ($\omega \propto R^{-0.4}$) and the fact that $J/M = p\omega R^2$, we can expect

[4] We note that this correlation is extremely tenuous. In a fit where each data point is weighted by the inverse of the square of its uncertainty, we find no significant correlation.

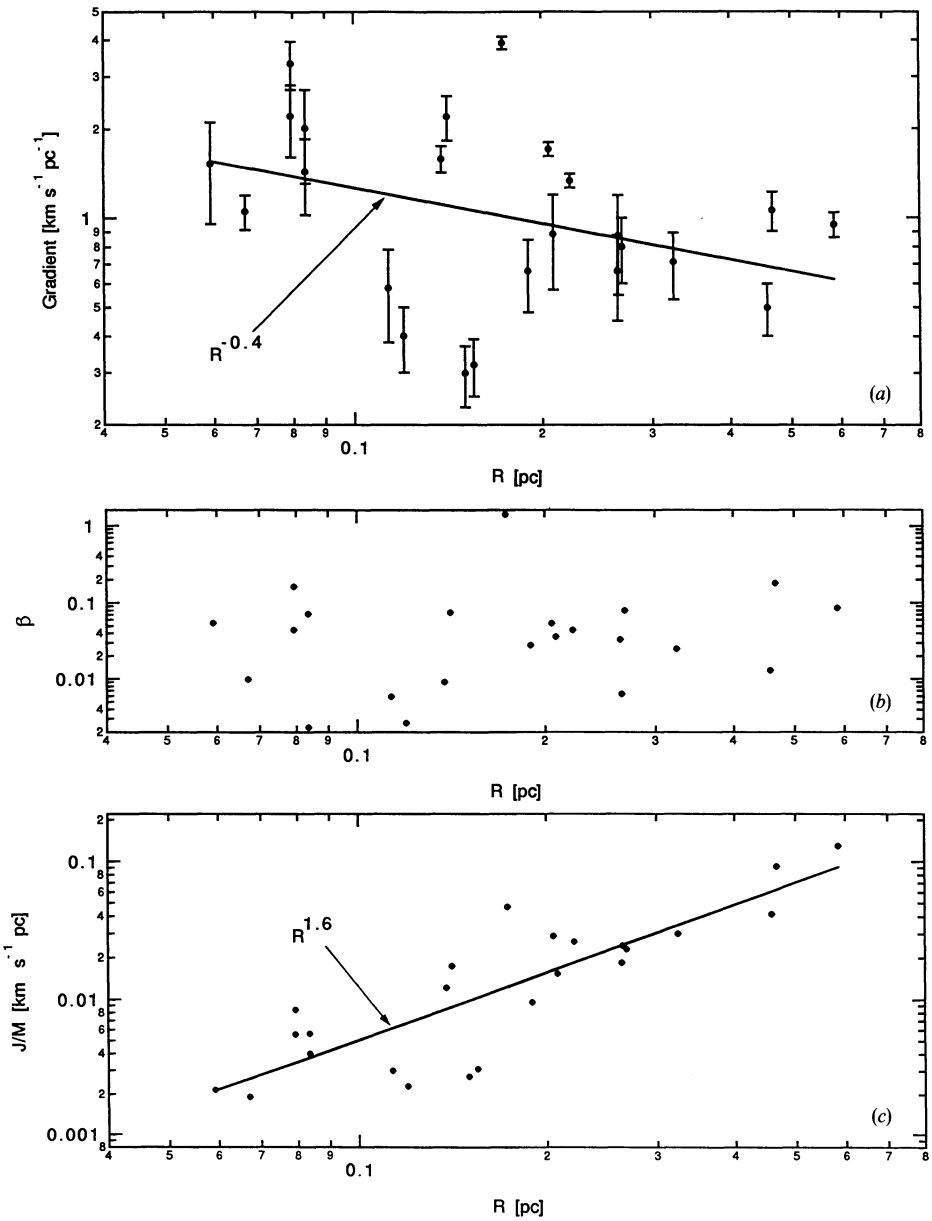

FIG. 13.—(*a*) Gradient magnitude, (*b*) β (calculated without any assumption of virial equilibrium), and (*c*) specific angular momentum as a function of cloud size. Best-fit lines are shown in (*a*) and (*c*). Errors on the fit parameters are given in the text.

the power-law correlation shown in Figure 13*c*

$$\frac{J}{M} = 10^{-0.7\pm0.2} R^{1.6\pm0.2} . \quad (11)$$

These scaling relations are very similar to those found by Goldsmith & Arquilla (1985), with their results systematically implying a somewhat larger amount of rotation than ours. Goldsmith & Arquilla (1985) caution that because their sample was selected as a group of rotating clouds, their findings often represent the "upper envelope" of rotation in dark clouds. We further caution that correlating J/M with R is not a fair comparison, given that the axes are not independent ($J/M \propto \omega R^2$). Any systematic dependence of ω on R will give a correlation of J/M and R: the true relation to study is the one between ω and R. And, if virial equilibrium holds, then the relation between ω and R depends only on $\beta^{1/2}$, and the real question becomes the study of the dependence (or lack thereof) of β on R.

6.6. *Is β Really Independent of Size?*

Why does it turn out that β is roughly independent of R in our analysis? One point bearing on this puzzle comes directly from examining our assumptions, and from equation (5). If one assumes, as we do in this paper, that ω and n are both independent of R, then $M \propto R^3$, and we see from equation (5) that β is automatically independent of R. Alternatively, if one assumes differential rotation ($\omega \propto R^{-1}$) rather than solid-body rotation (ω constant), and $M \propto R$ ($n \propto R^{-2}$), then β is again independent of R.

Thus, one possible consistent explanation for why the data in this paper imply that β does not depend on the size is

that NH_3 $(J, K) = (1, 1)$ emission actually does trace almost constant-density gas. As stated above, if this is true, then β is independent of R, with the assumption of constant ω. Observationally, there are many lines of evidence pointing toward NH_3 observations tracing a constant density (at least in "cold" cores, with kinetic temperature $\lesssim 15$ K). Even the finest single-dish NH_3 maps of cold low- to intermediate-mass dense cores (e.g., Figs. 6*a* and 6*b*; MW) show very little "internal structure" in the form of clumps within the cores. In general, NH_3 emission is not extended over a large range of size scales. On the larger scales, emission falls off rapidly, and on the smaller scales interferometric (VLA) NH_3 $(J, K) = (1, 1)$ observations often find no emission in cold cores because there are no structures in the map which have enough contrast not to be resolved out. And, when the volume density for cores mapped in the NH_3 $(J, K) = (1, 1)$ transition is derived from multiline fits, it is almost always with a factor of 5 of $10^{4.2}$ (see BM). We speculate that the small dynamic range which is apparently inherent in NH_3 observations allows us to map gas with approximately constant density, which in turn produces an apparent independence of β from R.

To learn the true size dependence of β, it is necessary to measure β as a function of size *in individual cores*, using several density tracers. Using such a technique, and assuming we can ever define just what an "individual core" is, it is likely that the size dependence of the role of rotation in the physics of a dense core will be described with less bias due to (density) selection effects.

6.7. *Comparison of J/M in Cores and Stars*

In lunar occultation observations of T Tauri stars, Simon et al. (1992) have measured the angular separation of 11 binary systems. From their results, M. Simon (1992, personal communication) has calculated J/M for the binary systems by assuming that each star has mass 0.5 $M_\odot$ and a circular orbit with respect to its companion. The distribution of J/M for the star systems ranges up to $\sim 10^{21}$ cm^2 s^{-1}, while the distribution of J/M presented here for cores, several of which are in Taurus, ranges down to 6×10^{20} cm^2 s^{-1}. Thus, there is no significant gap between the most rapidly rotating binary systems and the most slowly rotating cores. Therefore, these binaries and cores pose a much smaller "angular momentum problem" than do binaries and larger rotating clouds, or binaries and the differentially rotating disk of the Galaxy.

6.8. *What Determines ω?*

Theoretically, we need to understand just what key process, or processes, control the amount of rotation in any given cloud. Several mechanisms for governing angular momentum in the evolution of molecular clouds have been suggested thus far. The most popular choice, magnetic fields, which can control the motion of the predominantly neutral gas in a cloud through collisions with ions "tied" down to field lines anchored to the "stationary" ambient medium, provide an important interaction through so-called magnetic braking (cf. Königl 1987; Mouschovias 1991 and references therein). In addition, the fragmentation process in clouds could play a role in restricting the amount of angular momentum at any given size scale: when a cloud fragments, the angular momentum of the "children" is far less than that of their "parents," with the remainder going into the orbital energy of the resulting system (cf. Bodenheimer, Tohline, & Black 1980). It has even been proposed that the amount of rotation imparted to a cloud due to its immersion in a rotating galaxy could govern the so-called turbulent energy available to the cloud at the time of its formation (Fleck & Clark 1981), and thus perhaps the rotational energy available throughout the cloud's evolution. In reality, clouds are threaded by magnetic fields, *and* they fragment, *and* they form in a rotating galaxy, *and* they undergo other perhaps not yet considered processes, all of which conspire to regulate the amount of rotation in dense cores.

7. SUMMARY AND CONCLUSIONS

We summarize the key results of this paper as follows:

1. We have fitted linear gradients to the velocity field in more than 40 cores observed in the $(J, K) = (1, 1)$ transition of NH_3. In about two-thirds of the cases, the gradient fit is more than 3 times its uncertainty. In some cases we see that the relative motion of clumps, rather than continuous rotation, is responsible for the gradient observed. In other cases there is a smooth gradient across the map, and the cores may indeed be rotating, with constant angular speed. The magnitude of the gradients observed is small, ranging from 0.3 to 4 km s^{-1} pc^{-1}, with 1 km s^{-1} pc^{-1} being a typical value. The implied values of β, the ratio of rotational to gravitational energy, are also small, in comparison with earlier observations of larger clouds (e.g., Goldsmith & Arquilla 1985), ranging from 2×10^{-3} to 1.4, with typical values ~ 0.02.

2. Maps made in several different dense-gas tracers imply similar gradient directions.

3. *Gradient direction is not correlated with core elongation.* This finding is consistent with the ideas that at least some cores are prolate (Myers et al. 1991) and that rotation is not energetically dominant in the support of cores.

4. For two cores with extensive velocity maps (L43/RNO 90 and L1551), detailed analysis of the velocity field gives new information about core definition and outflows. The L43 dense core is kinematically distinct from the L43/RNO 90 NH_3 complex. Its gradient direction is clearly different from the gradient in the ambient gas, and the line widths in the core are much more alike than in the ambient gas. In L1551 the data of Menten & Walmsley (1985) show evidence in the NH_3 velocity field for outflow from the embedded star IRS 5, after removing the first-order gradient. The orientation of the outflow lobes and the signs of the velocity shift agree with CO and OH observations of the outflow. The velocity of what is apparently swept-up dense gas in L1551 is also consistent with prior observations, assuming a momentum-conserving wind.

5. The values of β we measure are generally smaller than the value ~ 0.15 needed to allow formation of binary stars by simple rotationally driven fission of a core into two pieces, each giving rise to one star. The smallest specific angular momentum we find in cores is 6×10^{20} cm^2 s^{-1}, slightly less than the largest (1×10^{21} cm^2 s^{-1}) found in pre–main-sequence binary star systems. This similarity indicates that some star-forming cores need not lose much angular momentum to form stellar systems. This conclusion differs from that based on comparisons of stellar and galactic rotation, which indicate an angular momentum "problem."

6. The specific angular momentum, J/M, increases with core size, R, roughly as $R^{1.5}$, as was also found by Goldsmith & Arquilla (1985). We note, though, that the dependence of J/M on R is not fundamental, as $J/M \propto \omega R^2$ by definition. For β roughly constant (i.e., independent of R), the dependence of ω

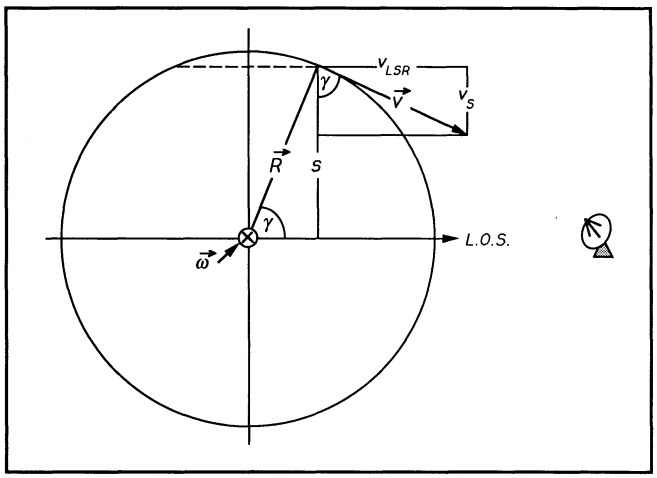

FIG. 14.—Schematic side view of solid-body rotation. The rotation axis points into the page, and the observer is to the right.

on R is predicted to be $\omega \propto R^{-0.5}$ for cores in virial equilibrium. Such a correlation between ω and R is marginally supported by the data presented here. However, because we have assumed constant density and gradient for any given core, it is difficult to know the true relation between β and core size.

We are grateful to A. Helmbock for his assistance with data processing, and we would like to thank F. Adams, P. Bodenheimer, A. Boss, M. Heyer, E. Ladd, C. McKee, M. Simon, S. Stahler, and M. Tafalla for insightful comments concerning this work. A. G. would also like to thank D. Plonsey for assistance in improving MONGO. P. J. B. is supported in part by NSF grant AST-8913001; G. A. F. is supported in part by a CfA Postdoctoral Fellowship; and A. A. G. is supported in part by a President's Fellowship at the University of California and NASA/ADP NAG-5-1230.

APPENDIX

This appendix is included to provide a clear illustration (Fig. 14) of why solid-body rotation of a gas cloud will give rise to a linear gradient in v_{LSR} across the face of a map, independent of optical depth.

In Figure 14, the observer is at the right, and ω points into the page. (We choose sin $i = 0$ here for convenience, but this analysis holds for arbitrary sin i.) The true velocity vector of any point in the cloud is given by

$$\boldsymbol{v} = \boldsymbol{\omega} \times \boldsymbol{R} , \tag{A1}$$

where $\boldsymbol{R}$ is a vector from the rotation axis to the point in question, lying in a plane perpendicular to ω. In the figure s represents the plane-of-the-sky component of $\boldsymbol{R}$, and thus

$$s = |\boldsymbol{R}| \sin \gamma , \tag{A2}$$

where γ is the angle between $\boldsymbol{R}$ and the line of sight. We can also think of s as representing an offset in a map, along the direction perpendicular to ω, defined by $\theta_{\mathcal{G}}$ in the text. The observed line-of-sight component of $\boldsymbol{v}$ will be

$$v_{LSR} = |\boldsymbol{v}| \sin \gamma . \tag{A3}$$

Thus, given that ω and $\boldsymbol{R}$ are defined to be perpendicular to each other, combining equations (A1)–(A3) gives

$$v_{LSR} = \omega s . \tag{A4}$$

So, from equation (A4), it is apparent that a constant value of ω will produce a linear gradient in v_{LSR} over a map, and that fitting a gradient ultimately amounts to finding the (plane-of-the-sky) orientation and magnitude of ω. Furthermore, since any point along the dashed cut through the cloud shown in Figure 14 will have the same value of s, the gradient determined from fitting v_{LSR} as a function of position on the sky (s) will be independent of optical depth. The only situation in which the gradient *will* be influenced by optical depth effects is the case where a consistent determination of v_{LSR} from point to point is not possible, due, for example, to irregular line profiles.

REFERENCES

Adams, F. C., & Shu, F. H. 1986, ApJ, 308, 836
Arcoragi, J.-P., Bonnell, I., Martel, H., Benz, W., & Bastien, P. 1991, ApJ, 380, 476
Armstrong, J. T., Ho, P. T. P., & Barrett, A. H. 1985, ApJ, 288, 159
Arquilla, R. 1984, Ph.D. thesis, Univ. Massachusetts, Amherst
Arquilla, R., & Goldsmith, P. F. 1985, ApJ, 297, 436 (AG85)
———. 1986, ApJ, 303, 356 (AG86)
Balázs, L. G., Eislöffel, J., Holl, A., Kelemen, J., & Kun, M. 1992, A&A, 255, 281
Bastien, P., Arcoragi, J.-P., Benz, W., Bonnell, I., & Martel, H. 1991, ApJ, 378, 255
Beichman, C. A., Myers, P. C., Emerson, J. P., Harris, S., Mathieu, R., Benson, P. J., & Jennings, R. E. 1986, ApJ, 307, 337
Benson, P. J. 1992, private communication

Benson, P. J., & Myers, P. C. 1989, ApJS, 71, 89 (BM)
Bevington, P. R. 1969, Data Reduction and Error Analysis for the Physical Sciences (New York: McGraw-Hill)
Bodenheimer, P., Tohline, J. E., & Black, D. C. 1980, ApJ, 242, 209
Bonnell, I., & Bastien, P. 1991, ApJ, 374, 610
Bonnell, I., Martel, H., Bastien, P., Arcoragi, J.-P., & Benz, W. 1991, ApJ, 377, 553
Boss, A. P. 1987, ApJ, 319, 149
———. 1988, ApJ, 331, 370
———. 1989, ApJ, 346, 336
Cassen, P., Shu, F. H., & Terebey, S. 1985, in Protostars and Planets II, ed. D. C. Black & M. S. Matthews (Tucson: Univ. Arizona Press), 448
Chandrasekhar, S. 1969, Ellipsoidal Figures of Equilibrium (New Haven: Yale Univ. Press)
Chandrasekhar, S., & Münch, G. 1950, ApJ, 111, 142
Cohen, M. 1980, AJ, 85, 29
Field, G. B. 1978, in Protostars and Planets, ed. T. Gehrels (Tucson: Univ. Arizona Press), 243
Fleck, R. C., & Clark, F. O. 1981, ApJ, 245, 898
Fuller, G. A. 1989, Ph.D. thesis, Univ. California, Berkeley
Fuller, G. A., Goodman, A. A., & Myers, P. C. 1993, in preparation
Fuller, G. A., Myers, P. C., Welch, W. J., Goldsmith, P. F., Langer, W. D., Campbell, B. G., Guilloteau, S., & Wilson, R. W. 1991, ApJ, 376, 135
Goldreich, P., & Lynden-Bell, D. 1965, MNRAS, 130, 97
Goldsmith, P. F., & Arquilla, R. 1985, in Protostars and Planets II, ed. D. C. Black & M. S. Matthews (Tucson: Univ. Arizona Press), 137
Goldsmith, P. F., & Sernyak, M. J., Jr. 1984, ApJ, 283, 140
Goodman, A. A., Bastien, P., & Myers, P. C. 1993, in preparation
Goodman, A. A., Bastien, P., Myers, P. C., & Ménard, F. 1990, ApJ, 359, 363
Hachisu, I., Tohline, J. E., & Eriguchi, Y. 1987, ApJ, 323, 592
Harris, A., Townes, C. H., Matsakis, D. N., & Palmer, P. 1983, ApJ, 265, L63
Heyer, M. H., Vrba, F. J., Snell, R. L., Schloerb, F. P., Strom, S. E., Goldsmith, P. F., & Strom, K. M. 1987, ApJ, 321, 855
Ho, P. T. P., & Haschick, A. D. 1986, ApJ, 304, 501
Ho, P. T. P., Moran, J. M., & Rodríguez, L. F. 1982, ApJ, 262, 619
Jackson, J. M., Ho, P. T. P., & Haschick, A. D. 1988, ApJ, 333, L73
Kiguchi, M., Narita, S., Miyama, S. M., & Hayashi, C. 1987, ApJ, 317, 830
Königl, A. 1987, ApJ, 320, 726
Ladd, E. F. 1991, Ph.D. thesis, Harvard Univ.
Landman, D. A., Roussel-Dupré, R., & Tanigawa, G. 1982, ApJ, 261, 732
Larson, R. B. 1981, MNRAS, 194, 809
Larson, R. B. 1985, MNRAS, 214, 379
Lizano, S., Heiles, C., Rodríguez, L. F., Koo, B.-C., Shu, F. H., Hasegawa, T., Hayashi, S., & Mirabel, I. F. 1988, ApJ, 328, 763
Mathieu, R. D., Benson, P. J., Fuller, G. A., Myers, P. C., & Schild, R. E. 1988, ApJ, 330, 385
Menten, K. M., & Walmsley, C. M. 1985, A&A, 146, 369 (MW)
Menten, K. M., Walmsley, C. M., Krügel, E., & Ungerechts, H. 1984, A&A, 137, 108
Mirabel, I. F., Rodríguez, L. F., Cantó, J., & Arnal, E. M. 1985, ApJ, 294, L39
Moriarty-Schieven, G. H., & Snell, R. L. 1988, ApJ, 332, 364
Mouschovias, T. C. 1991, ApJ, 373, 169
Myers, P. C. 1983, ApJ, 270, 105
Myers, P. C., & Benson, P. J. 1983, ApJ, 266, 309 (Paper II)
Myers, P. C., Fuller, G. A., Goodman, A. A., & Benson, P. J. 1991, ApJ, 376, 561 (Paper VI)
Myers, P. C., & Goodman, A. A. 1988, ApJ, 329, 392 (MG)
Nakano, T. 1984, Fund. Cosmic Phys., 9, 139
Pastor, J., Estalella, R., López, R., Anglada, G., Planesas, P., & Buj, J. 1993, A&A, in press
Sato, F., & Fukui, Y. 1989, ApJ, 343, 773
Schwartz, P. R., Gee, G., & Huang, Y.-L. 1988, ApJ, 327, 350
Shu, F. H., Adams, F. C., & Lizano, S. 1987, in ARA&A, 25, 23
Simon, M., Chen, W. P., Howell, R. R., Benson, J. A., & Slowik, D. 1992, ApJ, 384, 212
Snell, R. L., Loren, R. B., & Plambeck, R. L. 1980, ApJ, 239, L17
Stahler, S. 1983a, ApJ, 268, 155
———. 1983b, ApJ, 268, 165
Tamura, M., Gatley, I., Waller, W., & Werner, M. W. 1991, ApJ, 374, L25
Tassoul, J.-L. 1978, Theory of Rotating Stars (Princeton: Princeton Univ. Press)
Terebey, S., Shu, F. H., & Cassen, P. 1984, ApJ, 286, 529
Tomisaka, K. 1991, ApJ, 376, 190
Tomisaka, K., Ikeuchi, S., & Nakamura, T. 1988a, ApJ, 326, 208
———. 1988b, ApJ, 335, 239
———. 1989, ApJ, 341, 220
———. 1990, ApJ, 362, 202
Torrelles, J. M., Ho, P. T. P., Rodríguez, L. F., Cantó, J., & Moran, J. M. 1987, ApJ, 321, 884
Wadiak, E. J., Wilson, T. L., Rood, R. T., & Johnston, K. J. 1985, ApJ, 295, L43
Zheng, X. W., Ho, P. T. P., Reid, M. J., & Schneps, M. H. 1985, ApJ, 293, 522